



# Bending and stress responses of the hybrid axisymmetric system via state-space method and 3D-elasticity theory

Yinan Zhao<sup>1</sup> · Zohre Moradi<sup>2</sup> · Mohsen Davoudi<sup>2</sup> · Jinwu Zhuang<sup>1</sup>

Received: 21 October 2020 / Accepted: 12 December 2020 / Published online: 6 January 2021  
© The Author(s), under exclusive licence to Springer-Verlag London Ltd. part of Springer Nature 2021

## Abstract

This research presents bending responses of hybrid laminated nanocomposite reinforced axisymmetric circular/annular plates (HLNRACP/HLNRAAP) within the framework of non-polynomial under mechanical loading and various type of initially stresses via the three-dimensional elasticity theory. The current structure is on the Pasternak type of elastic foundation and torsional interaction. The state-space approach and differential quadrature method (SS-DQM) are studied to present the bending characteristics of the current structure by considering various boundary conditions. To predict the material properties of the bulk, the role of mixture and Halpin–Tsai equations are studied. For modeling the circular plate, a singular point is studied. Finally, a parametric study investigates the impacts of various types of distribution of laminated layers, stacking sequence on the stress/strain information of the HLNRACP/HLNRAAP. Results reveal that the system's static stability and bending behavior improve due to increasing the value of Winkler and Pasternak factors, and the stress distribution becomes more uniform.

**Keywords** Circumferential initially stresses · Linear and torsional gradient elastic foundation · 3D-elasticity theory · Bending · HLNRACP/HLNRAAP

## 1 Introduction

In the recent past years, a new horizon is presented by many researchers for using reinforcement materials because of that the materials provide a marvelous performance for different applicable complex structures [1–9]. One of the most well-known of these reinforcements is graphene nanoplatelets (GPLs) composite, which solved the mentioned demand [10]. With the aid of an experimental research, Rafiee et al.

[11] presented that using a little amount of GPLs in an epoxy basement could provide an impressive thermos mechanical properties compared with other reinforcements.

According to the mentioned applications, in the field of dynamic and static responses of the GPLRC structures, Hajilak et al. [12] provided a researcher about vibration and buckling behavior of the GPLRC shell reinforced with GPLs. They modeled a mathematical formulation by using modified strain gradient for considering size effects. Al-Furjan et al. [13] investigated the dynamic responses of the GPLRC disk with finite element and numerical models. They showed that as the amount of GPLs in an epoxy basement increases, the system's dynamic behavior could improve. Ebrahimi et al. [14] investigated wave responses of a GPLRC shell by considering imperfection or porosity and thermal environment. They showed that increasing the impacts of porosity and thermal environment could decrease the GPLs reinforced shell's stability. Habibi et al. [15] modeled an smart GPLs reinforced shell for investigation of wave propagation responses with the aid of strain radiant theory. They showed that due to increasing GPLs, the phase velocity and frequency of the mentioned system increase. In addition, the thermally affected GPLRC shell's

✉ Jinwu Zhuang  
hgzhaoyinan@163.com

Yinan Zhao  
1015084139@qq.com

Zohre Moradi  
z.moradi@edu.ikiu.ac.ir

Mohsen Davoudi  
davoudi@eng.ikiu.ac.ir

<sup>1</sup> College of Electric Engineering, Naval University of Engineering, Wuhan 430033, China

<sup>2</sup> Department of Electrical Engineering, Faculty of Engineering and Technology, Imam Khomeini International University, 34149-16818 Qazvin, Iran

static and dynamic stability are investigated by Safarpour et al. [16]. They presented the best pattern of GPLRC for having the highest frequency in the structure that is affected by a nonlinear thermal site and a foundation. By employing the differential quadrature method, Halpin–Tsai model, higher-order shear deformation, and proelasticity theories, Al-Furjan et al. [17] presented bending, static stability, and stress responses of a GPLs reinforced disk. Pourjabari et al. [18] presented a comprehensive study about free and forced vibration responses of the GPLs reinforced shell with the aid of modified strain gradient theory to consider the size effects. They reported three value for length scale parameters of the modified strain gradient theory. By using a semi numerical method Safarpour et al. [19] investigated the frequency responses of a GPLRC disk. Their results show that viscoelastic properties have an impressive impact on the system’s dynamics and the mentioned issue was more considerable at the higher value of GPLs weight fraction. Ebrahimi et al. [20] did research about the effects of GPLs patterns and porosity on the critical thermal loading and dynamic stability with the aid of modified couple stress theory for considering size effects. They showed that when the symmetric GPLs patterns are employed the structure could be able to encounter with the higher critical thermal loading. Habibi et al. [21] presented frequency of the smart GPLRC rotary nanoshell by using differential quadrature method, Halpin–Tsai model, and first-order shear deformation theory. They showed that the critical rotary speed of the smart structure could improve due to increasing the value of GPLs. Using the finite element method, Tam et al. [22] presented a research about nonlinear bending behaviors of a cracked GPLRC beam. they prove that when the crack depth and temperature of the environment increase, the strength of the structure decreases but this issue become negligible due to increasing GPLs weight fraction. Li et al. [23] showed bending responses of the GPLs reinforced plate with the aid of 2D approach and energy method. Liu et al. [24] studied the effects of six kinds of GPLs patterns on the linear free vibration and stress responses of the composite spherical shell based on 3D elasticity theory. Also, this material can be used in advanced structures and systems [25, 26]. A frequency up-conversion mechanism was suggested by Onsorynezhad et al. [27] to improve the performance of the piezoelectric energy harvester, and the mechanical and electrical behaviors of the energy harvester were analytically investigated. The frequency response results showed that the frequency up-conversion mechanism has significantly improved the energy harvester’s performance.

Furthermore, Wave responses, static and dynamic stability of different applicable complex and simple structures are investigated in many researches [28–40] with numerical and experimental methods. Based on the mentioned literature review, this is the first research to present bending responses

of hybrid laminated nanocomposite reinforced axisymmetric circular/annular plates within the framework of non-polynomial under mechanical loading and various type of initially stresses via the three-dimensional elasticity theory. The current structure is on the Pasternak type of elastic foundation and torsional interaction. The state-space approach along with differential quadrature method is studied to present the bending characteristics of the current structure by considering various boundary conditions. For predicting the material properties of the bulk, role of mixture and Halpin–Tsai equations are studied. For modeling the circular plate, a singular point is studied. Finally, a parametric study is done to investigate the impacts of various types of distribution of laminated layers, stacking sequence on the stress/strain information of the HLNRAAP/ HLNRAAP.

## 2 Mathematical modeling

In this research HLNRAAP reinforced by various distribution GPLs is presented. Based on the Halpin–Tsai model, have [41]

$$\bar{E} = \frac{1 + V_{GPL}\eta_W\xi_W}{1 - V_{GPL}\eta_W} \times \frac{5E_M}{8} + \frac{1 + \eta_L V_{GPL}\xi_L}{1 - V_{GPL}\eta_L} \times \frac{3E_M}{8}, \tag{1}$$

where  $\xi_L = 2 \frac{L_{GPL}}{t_{GPL}}$ ,  $\xi_W = 2 \frac{W_{GPL}}{t_{GPL}}$ ,  $V_{GPL}^* = \frac{\Lambda_{GPL}}{\Lambda_{GPL} + (\frac{\rho_{GPL}}{\rho_M})(1 - \Lambda_{GPL})}$ ,  $\eta_W = \frac{(\frac{E_{GPL}}{E_M}) - 1}{(\frac{E_{GPL}}{E_M}) + \xi_W}$  and  $\eta_L = \frac{(\frac{E_{GPL}}{E_M}) - 1}{(\frac{E_{GPL}}{E_M}) + \xi_L}$ .

Based on the following expression, the  $\bar{\nu}$  of the composite is as follows [42]

$$\bar{\nu} = \nu_M(1 - V_{GPL}) + V_{GPL}\nu_{GPL}. \tag{2}$$

For effective shear module have:

$$\bar{G} = \frac{E_C}{2(1 + \nu_C)}. \tag{3}$$

FG and uniform distribution of the laminated layers are formulated as below [41]

$$V_{GPL} = 4 \times \frac{1}{(V_{GPL}^*)^{-1}} \times |z_j| \times h^{-1} \quad \text{FG-X} \tag{4a}$$

$$V_{GPL} = 2 \times \frac{1}{(V_{GPL}^*)^{-1}} \times (1 - 2 \times |z_j| \times h^{-1}) \quad \text{FG-O} \tag{4b}$$

$$V_{GPL} = \frac{1}{(V_{GPL}^*)^{-1}} \times (1 - 2 \times |z_j| \times h^{-1}) \quad \text{FG-A} \tag{4c}$$

$$V_{GPL} = \frac{1}{(V_{GPL}^*)^{-1}} \times \left(1 + h^{-1} \times 2 \times |z_j|\right) \text{FG-V} \tag{4d}$$

$$V_{GPL} = \frac{1}{(V_{GPL}^*)^{-1}} \text{FG-UD} \tag{4e}$$

Here,  $z_j = \left(\frac{1}{2} + \frac{1}{2n} - \frac{j}{n}\right)h, \quad j = 1, 2, 3, \dots, n.$

### 2.1 Governing equations of the current structure

Figure 1 shows the geometry and coordinate of the current structure. 3D governing differential equation of motion by neglecting of body forces are [43–48]

$$\sigma_{r,r} + \tau_{rz,z} + r^{-1}\tau_{r\theta,\theta} - r^{-1}(\sigma_\theta + \sigma_r) + \sigma_0 r^{-2}(2u_{\theta,\theta} + u_r - u_{r,\theta\theta}) = 0 \tag{5a}$$

$$\tau_{r\theta,r} + r^{-1}\tau_{\theta z,\theta} + \sigma_{z,z} + 2r^{-1}\tau_{r\theta} + \sigma_0 r^{-2}(u_\theta - u_{\theta,\theta\theta} - 2u_{r,\theta}) = 0 \tag{5b}$$

$$\tau_{rz,r} + r^{-1}\tau_{\theta z,\theta} + \sigma_{z,z} + r^{-1}\tau_{rz} - \sigma_0 r^{-2}u_{z,\theta\theta} = 0 \tag{5c}$$

where bigger and smaller value of  $\sigma_0$  than zero means the compressive stress, and tensile stress, respectively. Stress–strain relations [49–51] of HLNRAAP reinforced by GPLs can be presented as follows:

$$\begin{Bmatrix} \sigma_{RR} \\ \sigma_{\theta\theta} \\ \sigma_{zz} \\ \tau_{z\theta} \\ \tau_{rz} \\ \tau_{r\theta} \end{Bmatrix} = \begin{bmatrix} \bar{Q}_{11} & \bar{Q}_{12} & \bar{Q}_{13} & 0 & 0 & 0 \\ \bar{Q}_{12} & \bar{Q}_{22} & \bar{Q}_{23} & 0 & 0 & 0 \\ \bar{Q}_{13} & \bar{Q}_{23} & \bar{Q}_{33} & 0 & 0 & 0 \\ & \text{sym.} & & \bar{Q}_{44} & 0 & 0 \\ & & & 0 & \bar{Q}_{55} & 0 \\ & & & 0 & 0 & \bar{Q}_{66} \end{bmatrix} \begin{Bmatrix} \epsilon_{RR} \\ \epsilon_{\theta\theta} \\ \epsilon_{zz} \\ \gamma_{z\theta} \\ \gamma_{rz} \\ \gamma_{r\theta} \end{Bmatrix} - \begin{Bmatrix} \gamma P \\ \gamma P \\ \gamma P \\ 0 \\ 0 \\ 0 \end{Bmatrix} \tag{6}$$

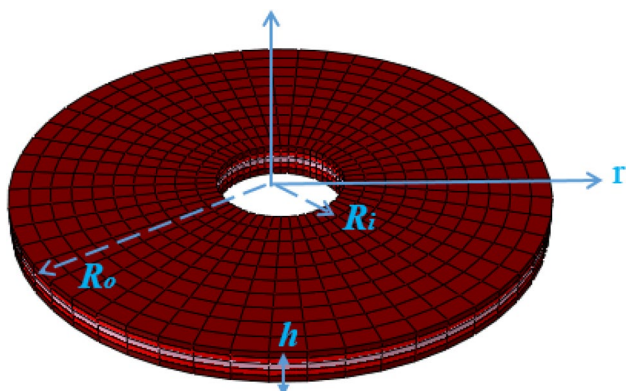


Fig. 1 Geometry and coordinate of the HLNRAAP

where the used parameters in Eq. (6) are presented in Refs. [52–61]. The strains of the HLNRAAP reinforced by GPLs can be given as [62]:

$$\epsilon_r = u_{r,r}, \quad \epsilon_\theta = r^{-1}(u_r + u_{\theta,\theta}), \quad \epsilon_z = u_{z,z}, \tag{7}$$

$$\gamma_{r\theta} = u_{\theta,r} + r^{-1}u_{r,\theta} - r^{-1}u_\theta, \quad \gamma_{rz} = u_{r,z} + u_{z,r}, \quad \gamma_{\theta z} = r^{-1}u_{z,\theta} + u_{\theta,z} \tag{8}$$

The other parameter in the Eq. (6) are as below:

$$P = \frac{(\psi - (\epsilon_{rr} + \epsilon_{\theta\theta} + \epsilon_{zz}))\gamma}{K^{-1}} \tag{9a}$$

$$K = -(k - k_u)\gamma^{-2} \tag{9b}$$

$$k_u = \left[1 - \frac{k_f \gamma^2}{(\phi - \gamma)(1 - \gamma)k_f + k_f \phi}\right] k \tag{9c}$$

In the Eq. (9a), parameter  $\psi = 0$  for un-drained conditions of fluid leads to:

$$P = -K\epsilon\gamma = -K(\epsilon_{rr} + \epsilon_{\theta\theta} + \epsilon_{zz})\gamma, \tag{10}$$

Now by substituting Eq. (10) into Eq. (6) gives

$$\sigma_{rr} = \bar{Q}_{13}^* u_{z,z} + r^{-1}\bar{Q}_{12}^*(u_r + u_{\theta,\theta}) + \bar{Q}_{11}^* u_{r,r} \tag{11a}$$

$$\sigma_{\theta\theta} = \bar{Q}_{23}^* u_{z,z} + \bar{Q}_{12}^* u_{r,r} + r^{-1}\bar{Q}_{22}^*(u_{\theta,\theta} + u_r) \tag{11b}$$

$$\sigma_{zz} = \bar{Q}_{33}^* u_{z,z} + r^{-1}\bar{Q}_{23}^*(u_r + u_{\theta,\theta}) + \bar{Q}_{13}^* u_{r,r} \tag{11c}$$

$$\tau_{\theta z} = \bar{Q}_{44}^*(r^{-1}u_{z,\theta} + u_{\theta,z}) \tag{11d}$$

$$\tau_{rz} = \bar{Q}_{55}^*(u_{z,r} + u_{r,z}) \tag{11e}$$

$$\tau_{r\theta} = \bar{Q}_{66}^*(r^{-1}u_{r,\theta} - r^{-1}u_\theta + u_{\theta,r}), \tag{11f}$$

where

$$\bar{Q}_{11}^* = \frac{K}{\gamma^{-2}} + \bar{Q}_{11} \tag{12a}$$

$$\bar{Q}_{12}^* = \frac{K}{\gamma^{-2}} + \bar{Q}_{12} \tag{12b}$$

$$\bar{Q}_{13}^* = \frac{K}{\gamma^{-2}} + \bar{Q}_{13} \tag{12c}$$

$$\bar{Q}_{22}^* = \frac{K}{\gamma^{-2}} + \bar{Q}_{22} \tag{12d}$$

$$\bar{Q}_{23}^* = \frac{K}{\gamma^{-2}} + \bar{Q}_{23} \tag{12e}$$

$$\bar{Q}_{33}^* = \frac{K}{\gamma^{-2}} + \bar{Q}_{33} \tag{12f}$$

Using Eqs. (5a–c) and (11a–f):

$$\frac{\partial u_r}{\partial z} = -u_{z,r} + \frac{\tau_{rz}}{Q_{55}} \tag{13a}$$

$$\frac{\partial u_\theta}{\partial z} = -\frac{u_{z,\theta}}{r} + \frac{\tau_{z\theta}}{Q_{44}} \tag{13b}$$

$$\frac{\partial u_z}{\partial z} = -\frac{\bar{Q}_{13}^*}{\bar{Q}_{33}^*} u_{r,r} - r^{-1} \frac{\bar{Q}_{23}^*}{\bar{Q}_{33}^*} u_r - r^{-1} \frac{\bar{Q}_{23}^*}{\bar{Q}_{33}^*} u_{\theta,\theta} + \frac{\sigma_z}{\bar{Q}_{33}^*} \tag{13c}$$

$$\frac{\partial \sigma_z}{\partial z} = r^{-2} \sigma_0 u_{z,\theta\theta} - \tau_{rz,r} - r^{-1} \tau_{rz} + r^{-1} \tau_{z,\theta\theta} \tag{13d}$$

$$\begin{aligned} \frac{\partial \tau_{rz}}{\partial z} = & - \left( \frac{\bar{Q}_{11}^*}{\bar{Q}_{33}^*} - \frac{\bar{Q}_{13}^{*2}}{\bar{Q}_{33}^*} \right) u_{r,rr} + r^{-2} \sigma_0 (u_{r,\theta\theta} - 2u_{\theta,\theta} - u_r) - r^{-1} \left( \frac{\bar{Q}_{11}^*}{\bar{Q}_{33}^*} - \frac{\bar{Q}_{13}^{*2}}{\bar{Q}_{33}^*} \right) u_{r,r} - r^{-2} \bar{Q}_{66} u_{r,\theta\theta} \\ & - \frac{\bar{Q}_{13}^*}{\bar{Q}_{33}^*} \sigma_{z,r} - \left( \frac{\bar{Q}_{13}^* - \bar{Q}_{23}^*}{\bar{Q}_{33}^*} \right) \sigma_z - r^{-2} \left( \frac{\bar{Q}_{12}^* \bar{Q}_{33}^* + \bar{Q}_{23}^{*2} - \bar{Q}_{13}^* \bar{Q}_{23}^* - \bar{Q}_{22}^* \bar{Q}_{33}^*}{\bar{Q}_{33}^*} \right) u_r \\ & - r^{-1} \left( \frac{\bar{Q}_{12}^* + \bar{Q}_{66} - \frac{\bar{Q}_{13}^* \bar{Q}_{23}^*}{\bar{Q}_{33}^*}}{\bar{Q}_{33}^*} \right) u_{\theta,r\theta} - r^{-2} \left( \frac{\bar{Q}_{12}^* \bar{Q}_{33}^* + \bar{Q}_{23}^{*2} - \bar{Q}_{13}^* \bar{Q}_{23}^* - \bar{Q}_{22}^* \bar{Q}_{33}^*}{\bar{Q}_{33}^*} \right) u_{\theta,\theta} \end{aligned} \tag{13e}$$

$$\begin{aligned} \frac{\partial \tau_{\theta z}}{\partial z} = & -r^{-1} \left( \frac{\bar{Q}_{12}^*}{\bar{Q}_{33}^*} + \bar{Q}_{66} - \frac{\bar{Q}_{13}^* \bar{Q}_{23}^*}{\bar{Q}_{33}^*} \right) u_{r,r\theta} - r^{-2} \left( \frac{\bar{Q}_{22}^*}{\bar{Q}_{33}^*} + 2\bar{Q}_{66} - \frac{\bar{Q}_{23}^{*2}}{\bar{Q}_{33}^*} \right) u_{r,\theta} \\ & - \bar{Q}_{66} u_{\theta,rr} - \frac{\bar{Q}_{66}}{r} u_{\theta,r} - r^{-2} \left( \frac{\bar{Q}_{22}^*}{\bar{Q}_{33}^*} - \frac{\bar{Q}_{23}^{*2}}{\bar{Q}_{33}^*} \right) u_{\theta,\theta\theta} \\ & + 2r^{-2} \bar{Q}_{66} u_\theta + r^{-2} \sigma_0 (2u_{r,\theta} + u_{\theta,\theta\theta} - u_\theta) - r^{-1} \frac{\bar{Q}_{23}^*}{\bar{Q}_{33}^*} \sigma_{z,\theta} \end{aligned} \tag{13f}$$

where  $\delta = \{u_r, u_\theta, u_z, \sigma_z, \tau_{rz}, \tau_{\theta z}\}^T$ .

And the relations for different boundary conditions can be formulated as follows:

Simply :  $\sigma_r = u_z = u_\theta = 0$     Clamped :  $u_z = u_r = u_\theta = 0$ . (15)

Also, for a circular plate at  $r=0$ :

$$u_{z,r} = u_r = 0 \quad r = 0 \tag{16}$$

### 3 Applying linear and torsional elastic foundation

The Winkler–Pasternak foundations for HLNRACP/ HLN-RAAP reinforced by GPLs can be formulated as:

$$\chi = -r^{-1} (ru_{z,r} k_p(r, \theta, z))_{,r} - r^{-2} (u_{z,\theta} k_p(r, \theta, z))_{,r} + k_w(r, \theta, z) u_z \tag{17}$$

The used parameters in Eq. (17) can be given as:

$$k_w(r, \theta, z) = k_{wo} (1 + f_1 r r_o + f_2 r^2 r_o^{-2}) \cos(\theta_0) \tag{18a}$$

$$k_p(r, \theta, z) = k_{po} (1 + f_1 r r_o + f_2 r^2 r_o^{-2}) \cos(\theta_0). \tag{18b}$$

The form of matrix of Eqs. (13a–f) can be written as:

$$\frac{d\delta}{dz} = G\delta, \tag{14}$$

The torsional elastic foundation can be formulated as:

$$\chi_r = k_{r1}(r, \theta)\phi - r^{-1} (r\phi_{,r} k_{r2}(r, \theta))_{,r}, \tag{19}$$

Substituting  $\phi = \partial u_\theta / \partial r$  into Eq. (20) gives:

$$\chi_r = k_{r1}(r, \theta)u_{\theta,r} - r^{-1}(ru_{\theta,rr}k_{r2}(r, \theta))_{,r} \tag{20}$$

These coefficients are considered as

$$k_{r1}(r, \theta) = (1 + f_1rr_o + f_2r^2r_o^{-2})k_{r10} \sin(\theta_0) \tag{21a}$$

$$k_{r2}(r, \theta, z) = (1 + f_1rr_o + f_2r^2r_o^{-2})k_{r20} \sin(\theta_0). \tag{21b}$$

### 3.1 Solution procedure

To date, many studies showed that computer and numerical methods [63–72] are highly used for modeling different phenomena. In this research for solving the governing equations we apply DQM that have [19, 73]:

$$\frac{\partial^n f}{\partial r^n} = \sum_{m=1}^M g_{j,m}^{(n)} f_{m,k}, \tag{22}$$

here,  $g^{(n)}$ , can be extracted as below:

$$g_{ij}^{(1)} = - \sum_{j=1, i \neq j}^n g_{ij}^{(1)} \quad i = j \tag{23}$$

$$g_{ij}^{(1)} = \frac{M(x_i)}{(x_i - x_j)M(x_j)} \quad i, j = 1, 2, \dots, n \text{ and } i \neq j,$$

where:

$$M(x_i) = \prod_{j=1, j \neq i}^n (x_i - x_j). \tag{24}$$

The derivatives of Eq. (24) can be written as the following equations [74]:

$$g_{ii}^{(n)} = - \sum_{j=1, i \neq j}^n g_{ij}^{(n)} \quad 1 \leq n \leq N - 1 \text{ while } j, i = 1, 2, \dots, N$$

$$g_{ij}^{(n)} = r \left[ g_{ij}^{(n-1)} g_{ij}^{(1)} - \frac{g_{ij}^{(n-1)}}{(x_i - x_j)} \right] \quad i \neq j, 2 \leq n \leq N - 1 \text{ while } j, i = 1, 2, \dots, N. \tag{25}$$

In addition, via greed points of Chebyshev polynomials, the seed along with r-axes is as follows:

$$r_i = \frac{R_0 - R_i}{2} \left( 1 - \cos \left( \frac{(i-1)\pi}{(N_i-1)} \right) \right) + R_i \quad i = 1, 2, 3, \dots, N_i. \tag{26}$$

Besides, displacement fields of the HLN-RACP/ HLN-RAAP reinforced by GPLs are as:

$$u_r = \sum_{m=1}^{\infty} \hat{u}_r \sin(\theta P_m), u_{\theta} = \sum_{m=1}^{\infty} \hat{u}_{\theta} \cos(\theta P_m), u_z = \sum_{m=1}^{\infty} \hat{u}_z \sin(\theta P_m), \tag{27a}$$

$$\sigma_r = \sum_{m=1}^{\infty} \hat{\sigma}_r \sin(\theta P_m), \sigma_{\theta} = \sum_{m=1}^{\infty} \hat{\sigma}_{\theta} \sin(\theta P_m), \sigma_z = \sum_{m=1}^{\infty} \hat{\sigma}_z \sin(\theta P_m), \tag{27b}$$

$$\tau_{rz} = \sum_{m=1}^{\infty} \hat{\tau}_{rz} \sin(\theta P_m), \tau_{r\theta} = \sum_{m=1}^{\infty} \hat{\tau}_{r\theta} \cos(\theta P_m),$$

$$\tau_{\theta z} = \sum_{m=1}^{\infty} \hat{\tau}_{\theta z} \cos(\theta P_m), \tag{27c}$$

where:  $P_m = m$ . We assumed, the following dimensionless form of equations:

$$\bar{E} = \frac{E}{P_0}, \quad (\bar{\sigma}_z \bar{\sigma}_r \bar{\sigma}_{\theta} \bar{\tau}_{rz} \bar{\tau}_{r\theta} \bar{\tau}_{\theta z}) = \frac{1}{E_m} (\hat{\sigma}_z \hat{\sigma}_r \hat{\sigma}_{\theta} \hat{\tau}_{rz} \hat{\tau}_{r\theta} \hat{\tau}_{\theta z}) \tag{28a}$$

$$\bar{r} = \frac{r}{R_m}, \quad (\bar{U}_r \bar{U}_{\theta} \bar{U}_z) = \frac{1}{h} (u_r \ u_{\theta} \ u_z),$$

$$S = \frac{h}{R_m}, \quad \bar{Z} = \frac{Z}{h}, \quad \bar{P}_m = P_m \tag{28b}$$

$$P_0 = 1 \text{ [Mpa]}, \quad \bar{p} = \frac{q}{P_0}, \quad \bar{g}_{ij} = g_{ij} R_m, \quad \hat{Q}_{ij} = \frac{\bar{Q}_{ij}}{P_0}, \quad \bar{\sigma}_0 = \frac{\sigma_0}{P_0}. \tag{28c}$$

Substitution of Eqs. (28a–b), (27a–b) and (22) into Eq. (14):

$$\frac{\partial \bar{u}_{ri}}{\partial \bar{z}} = -S \sum_{j=1}^N \bar{g}_{ij} \bar{u}_{zj} + \frac{\bar{\tau}_{rzi}}{\hat{Q}_{55}} \tag{29a}$$

$$\frac{\partial \bar{u}_{\theta i}}{\partial \bar{z}} = -S \bar{r}_i^{-1} P_m \bar{u}_{zi} + \frac{\bar{\tau}_{z\theta i}}{\hat{Q}_{44}} \tag{29b}$$

$$\frac{\partial \bar{u}_{zi}}{\partial \bar{z}} = \frac{\bar{\sigma}_{zi}}{\hat{Q}_{33}} - S \frac{\hat{Q}_{13}}{\hat{Q}_{33}} \sum_{j=1}^N \bar{g}_{ij} \bar{u}_{rj} - S \bar{r}_i^{-1} \frac{\hat{Q}_{23}}{\hat{Q}_{33}} \bar{u}_{ri} + S \bar{r}_i^{-1} \frac{P_m \hat{Q}_{23}}{\hat{Q}_{33}} \bar{u}_{\theta i} \tag{29s}$$

$$\frac{\partial \bar{\sigma}_{zi}}{\partial \bar{z}} = -r_i^{-2} \sigma_0 P_m^2 \bar{u}_{zi} - S \sum_{j=1}^N \bar{g}_{ij} \bar{\tau}_{r_{zj}} - S \bar{r}_i^{-1} \bar{\tau}_{r_{zi}} - S \bar{r}_i^{-1} P_m \bar{\tau}_{z\theta i}, \tag{29d}$$

By using a layer-wise technique,  $\bar{G}_b$  is decreased to the constant matrix and finally Eq. (31) can be solved analytically for  $N_t$  fictitious layer as the follows

$$\begin{aligned} \frac{\partial \bar{\tau}_{r_{zi}}}{\partial \bar{z}} = & -S \frac{\hat{Q}_{13}}{\hat{Q}_{33}} \sum_{j=1}^N g_{ij} \sigma_{zj} - S \bar{r}_i^{-1} \left( \frac{\hat{Q}_{13} - \hat{Q}_{23}}{\hat{Q}_{33}} \right) \sigma_{zi} - S^2 \left( \hat{Q}_{11} - \frac{\hat{Q}_{13}^2}{\hat{Q}_{33}} \right) \sum_{j=1}^N \bar{g}_{ij}^2 \bar{u}_{rj} \\ & - S^2 \bar{r}_i^{-1} \left( \hat{Q}_{11} - \frac{\hat{Q}_{13}^2}{\hat{Q}_{33}} \right) \sum_{j=1}^N \bar{g}_{ij} \bar{u}_{rj} + P_m^2 \bar{r}_i^{-2} \hat{Q}_{66} \bar{u}_{ri} + \sigma_0 \bar{r}_i^{-2} (P_m^2 \bar{u}_{ri} - 2P_m \bar{u}_{\theta i} + \bar{u}_{ri}) \\ & - S^2 \bar{r}_i^{-2} \left( \frac{\hat{Q}_{12} \hat{Q}_{33} + \hat{Q}_{23}^2 - \hat{Q}_{13} \hat{Q}_{23} - \hat{Q}_{22} \hat{Q}_{33}}{\hat{Q}_{33}} \right) \bar{u}_{ri} \\ & + S^2 \bar{r}_i^{-1} P_m \left( \hat{Q}_{12} + \hat{Q}_{66} - \frac{\hat{Q}_{13} \hat{Q}_{23}}{\hat{Q}_{33}} \right) \sum_{j=1}^N \bar{g}_{ij} \bar{u}_{\theta j} \\ & + S^2 \bar{r}_i^{-2} P_m^2 \left( \frac{\hat{Q}_{12} \hat{Q}_{33} + \hat{Q}_{23}^2 - \hat{Q}_{13} \hat{Q}_{23} - \hat{Q}_{22} \hat{Q}_{33}}{\hat{Q}_{33}} \right) \bar{u}_{\theta i} \end{aligned} \tag{29e}$$

$$\begin{aligned} \frac{\partial \bar{\tau}_{\theta zi}}{\partial \bar{z}} = & -S \frac{P_m}{\bar{r}_i} \frac{\hat{Q}_{23}}{\hat{Q}_{33}} \bar{\sigma}_{zi} - S^2 \frac{P_m}{\bar{r}_i} \left( \hat{Q}_{12} + \hat{Q}_{66} - \frac{\hat{Q}_{13} \hat{Q}_{23}}{\hat{Q}_{33}} \right) \sum_{j=1}^N \bar{g}_{ij} \bar{u}_{rj} \\ & - S^2 \frac{P_m}{\bar{r}_i} \left( \hat{Q}_{22} + 2\hat{Q}_{66} - \frac{\hat{Q}_{23}^2}{\hat{Q}_{33}} \right) \bar{u}_{ri} - S^2 \hat{Q}_{66} \sum_{j=1}^N \bar{g}_{ij}^2 \bar{u}_{\theta j} - S^2 \frac{\hat{Q}_{66}}{\bar{r}_i} \sum_{j=1}^N \bar{g}_{ij} \bar{u}_{\theta j} \\ & + S^2 \frac{P_m^2}{\bar{r}_i^2} \left( \hat{Q}_{22} - \frac{\hat{Q}_{23}^2}{\hat{Q}_{33}} \right) \bar{u}_{\theta i} + S^2 \frac{2\hat{Q}_{66}}{\bar{r}_i^2} \bar{u}_{\theta i} + \frac{\sigma_0}{\bar{r}_i^2} (2P_m \bar{u}_{ri} - P_m^2 \bar{u}_{\theta i} - \bar{u}_{\theta i}), \end{aligned} \tag{29f}$$

where:

$$\bar{u}_{ki} = \bar{u}_k(r, \theta, z); \quad (k = r_i, \theta, z), \quad \bar{\sigma}_{ki} = \bar{\sigma}_k(r, \theta, z), \quad \bar{\tau}_{\theta zi} = \bar{\tau}_{\theta z}(r, \theta, z), \quad \bar{\tau}_{r_{zi}} = \bar{\tau}_{r_z}(r, \theta, z) \tag{30}$$

Substitution of Eqs. (15)–(16) into Eqs. (29a–f) gives the following state-space equations

$$\frac{\partial \bar{\delta}_b}{\partial \bar{z}} = \bar{G}_b \bar{\delta}_b, \tag{31}$$

where  $\bar{\delta}_b = \{ \bar{u}_r \ \bar{u}_\theta \ \bar{u}_z \ \bar{\sigma}_z \ \bar{\tau}_{r_z} \ \bar{\tau}_{\theta z} \}^T$  is the column matrix of state variables. In addition, subscript, b in Eq. (31) denotes the state equation includes the boundary conditions [38, 75, 76].

$$\delta_k(\bar{z}) = \delta_{ok} \exp \left( \bar{G}_{bk} (\bar{z} - \bar{z}_{k-1}) \right), \quad \bar{z}_{k-1} \leq \bar{z} \leq \bar{z}_k. \tag{32}$$

At the inner and outer radius of  $k$ th layer, the relation between the state variables can be given as follows:

$$\delta_k(\bar{z}_k) = \bar{M}_k \delta_{ok}. \tag{33}$$

In which  $\bar{M}_k = \exp \left( \frac{\bar{G}_{bk} \bar{h}_k}{N_t} \right)$ .

**Table 1** Compare the  $\bar{w}_0^F(0, 0)$  of functionally graded clamped circular plates with the result in Ref. [79]

n	h/a=0.05		h/a=0.1		h/a=0.15		h/a=0.2	
	Ref. [79]	PS	Ref. [79]	PS	Ref. [79]	PS	Ref. [79]	PS
0	2.554	2.8702	2.639	2.9195	2.781	3.1057	2.979	3.2186
2	1.402	1.5820	1.444	1.6081	1.515	1.6962	1.613	1.8903
4	1.282	1.4483	1.320	1.4727	1.384	1.5513	1.473	1.6545
6	1.220	1.3796	1.257	1.4037	1.318	1.4792	1.404	1.5656
8	1.181	1.3366	1.217	1.3605	1.278	1.4348	1.362	1.5625
10	1.155	1.3070	1.190	1.3307	1.250	1.4043	1.333	1.5641
15	1.114	1.2621	1.149	1.2853	1.208	1.3584	1.289	1.4750
20	1.092	1.2369	1.126	1.2597	1.184	1.3326	1.265	1.3996
25	1.077	1.2208	1.112	1.2433	1.169	1.3162	1.250	1.4209
30	1.067	1.2096	1.101	1.2319	1.159	1.3047	1.239	1.3555
35	1.060	1.2014	1.094	1.2235	1.151	1.2964	1.231	1.3583
40	1.054	1.1952	1.088	1.2170	1.145	1.2900	1.225	1.4598
50	1.046	1.1903	1.080	1.2119	1.137	1.2850	1.216	1.3685
10 <sup>2</sup>	1.029	1.1863	1.063	1.2078	1.119	1.2810	1.199	1.3925
10 <sup>3</sup>	1.013	1.1683	1.047	1.1892	1.103	1.2624	1.182	1.3448
10 <sup>4</sup>	1.011	1.1569	1.045	1.1773	1.101	1.2508	1.180	1.3012
10 <sup>5</sup>	1.011	1.1569	1.045	1.1773	1.101	1.2508	1.180	1.3880

### 3.2 Static analysis

Whereas for static analysis it is assumed following surface traction boundary condition.

$$\begin{aligned} \bar{\sigma}_z = \chi, \quad \bar{\tau}_{rz} = 0, \quad \bar{\tau}_{\theta z} = \chi_r \quad & \text{at } \bar{z} = -\frac{1}{2} \\ \bar{\sigma}_z = \bar{p} \cos(\theta_0), \quad \bar{\tau}_{rz} = \bar{\tau}_{\theta z} = 0 \quad & \text{at } \bar{z} = \frac{1}{2}. \end{aligned} \tag{34}$$

Applying Eqs. (33) and (34) gives the following homogenous equation:

$$\bar{\sigma}_{ri} = \frac{\hat{Q}_{13}}{\hat{Q}_{33}} \bar{\sigma}_{zi} + S \left( \frac{\hat{Q}_{11}}{\hat{Q}_{33}} - \frac{\hat{Q}_{13}^2}{\hat{Q}_{33}^2} \right) \sum_{j=1}^N \bar{g}_{ij} \bar{u}_{rj} + S r_i^{-1} \left( \frac{\hat{Q}_{12}}{\hat{Q}_{33}} - \frac{\hat{Q}_{13} \hat{Q}_{23}}{\hat{Q}_{33}^2} \right) (\bar{u}_{ri} - P_m \bar{u}_{\theta i}) \tag{36a}$$

$$\bar{\sigma}_{\theta i} = \frac{\hat{Q}_{23}}{\hat{Q}_{33}} \bar{\sigma}_{zi} + S \left( \frac{\hat{Q}_{12}}{\hat{Q}_{33}} - \frac{\hat{Q}_{13} \hat{Q}_{23}}{\hat{Q}_{33}^2} \right) \sum_{j=1}^N \bar{g}_{ij} \bar{u}_{rj} + S r_i^{-1} \left( \frac{\hat{Q}_{22}}{\hat{Q}_{33}} - \frac{\hat{Q}_{23}^2}{\hat{Q}_{33}^2} \right) (\bar{u}_{ri} - P_m \bar{u}_{\theta i}) \tag{36b}$$

$$\begin{bmatrix} \lambda_{12} & \lambda_{13} + \lambda_{16} \chi_r & \lambda_{14} + \lambda_{11} \chi \\ \lambda_{52} & \lambda_{53} + \lambda_{56} \chi_r & \lambda_{54} + \lambda_{51} \chi \\ \lambda_{62} & \lambda_{63} + \lambda_{66} \chi_r & \lambda_{64} + \lambda_{61} \chi \end{bmatrix} \begin{Bmatrix} \bar{u}_r \\ \bar{u}_\theta \\ \bar{u}_z \end{Bmatrix} \Big|_{\bar{z}=-\frac{1}{2}} = \begin{Bmatrix} \bar{p} \cos(\theta_0) \\ 0 \\ 0 \end{Bmatrix} \Big|_{\bar{z}=\frac{1}{2}}.$$

In addition,  $\bar{p} = \{\bar{p}_1, \dots, \bar{p}_N\}^T$ . Displacements at the bottom surface can be obtained by solving Eq. (35) and then by using Eq. (33) transverse normal and shear stresses as well as displacements as a function of radial coordinated are determined. Finally, in-plane normal and shear stresses are computed from the following equations;

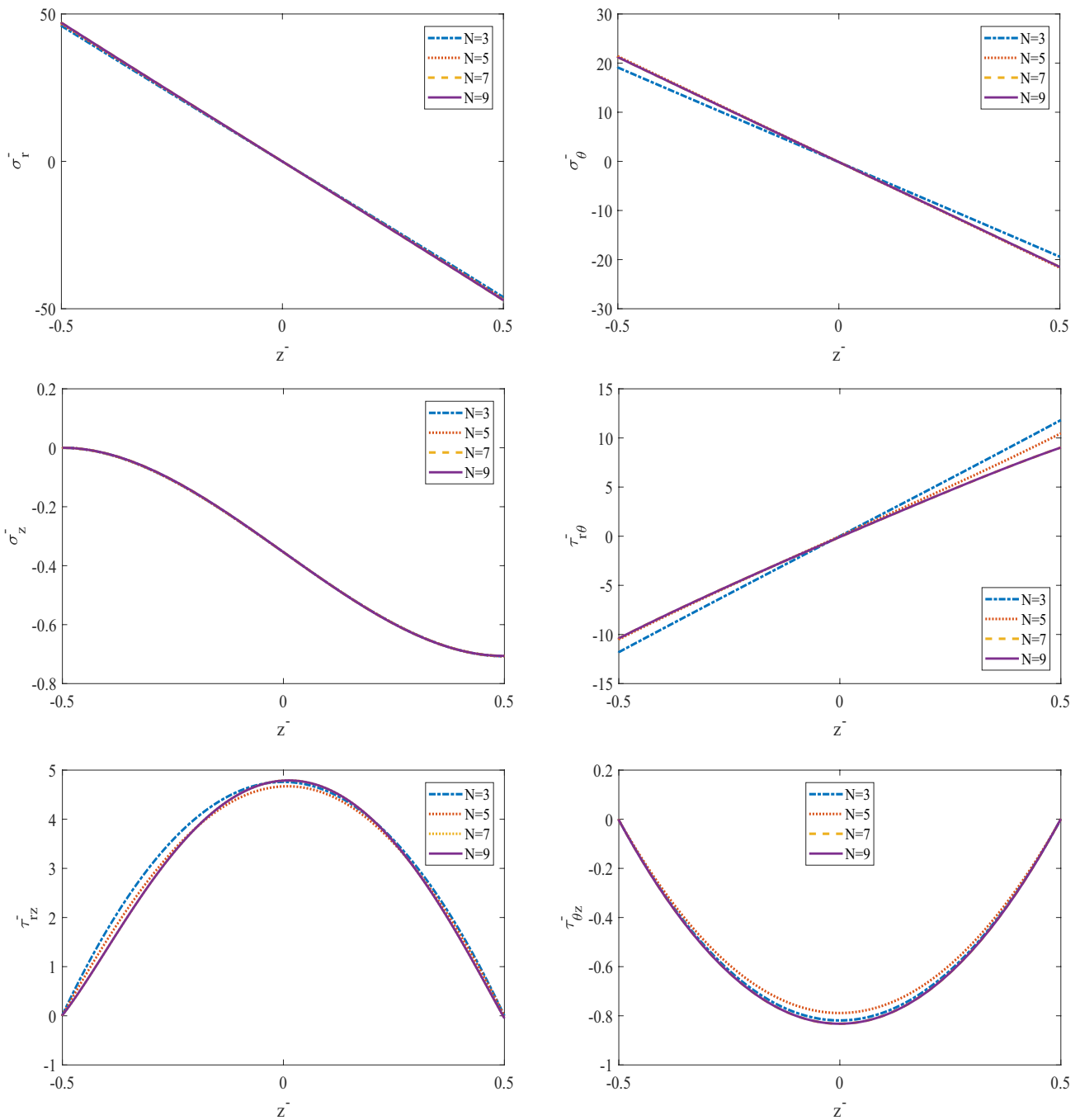


**Fig. 2** Convergence number of grid points for an investigation of the displacement and stress fields of the FG-GPLRC annular plates.  $R_i=0.5$ ,  $R_o=2R_i$ ,  $h=0.1R_i$ ,  $\Lambda_{GPL} = 1$  (wt%), GPL-UD,

$K_{wo}=K_{po}=100$ ,  $f_1=f_2=0.1$ ,  $K_{r10}=K_{r20}=100$ ,  $\theta_0 = \pi/4$ ,  $\theta_0 = \pi/4$  and Simply–Simply boundary conditions

$$\bar{\tau}_{r\theta i} = S\bar{r}_i^{-1} P_m \hat{Q}_{66} u_{ri} + S\hat{Q}_{66} \sum_{j=1}^N \bar{g}_{ij} \bar{u}_{\theta j} + S\bar{r}_i^{-1} \hat{Q}_{66} \bar{u}_{\theta i}. \quad (36c)$$

### 4 Result

Material properties of graphene nanoplates, matrix, and the poroelastic constants are presented in Refs. [77, 78].



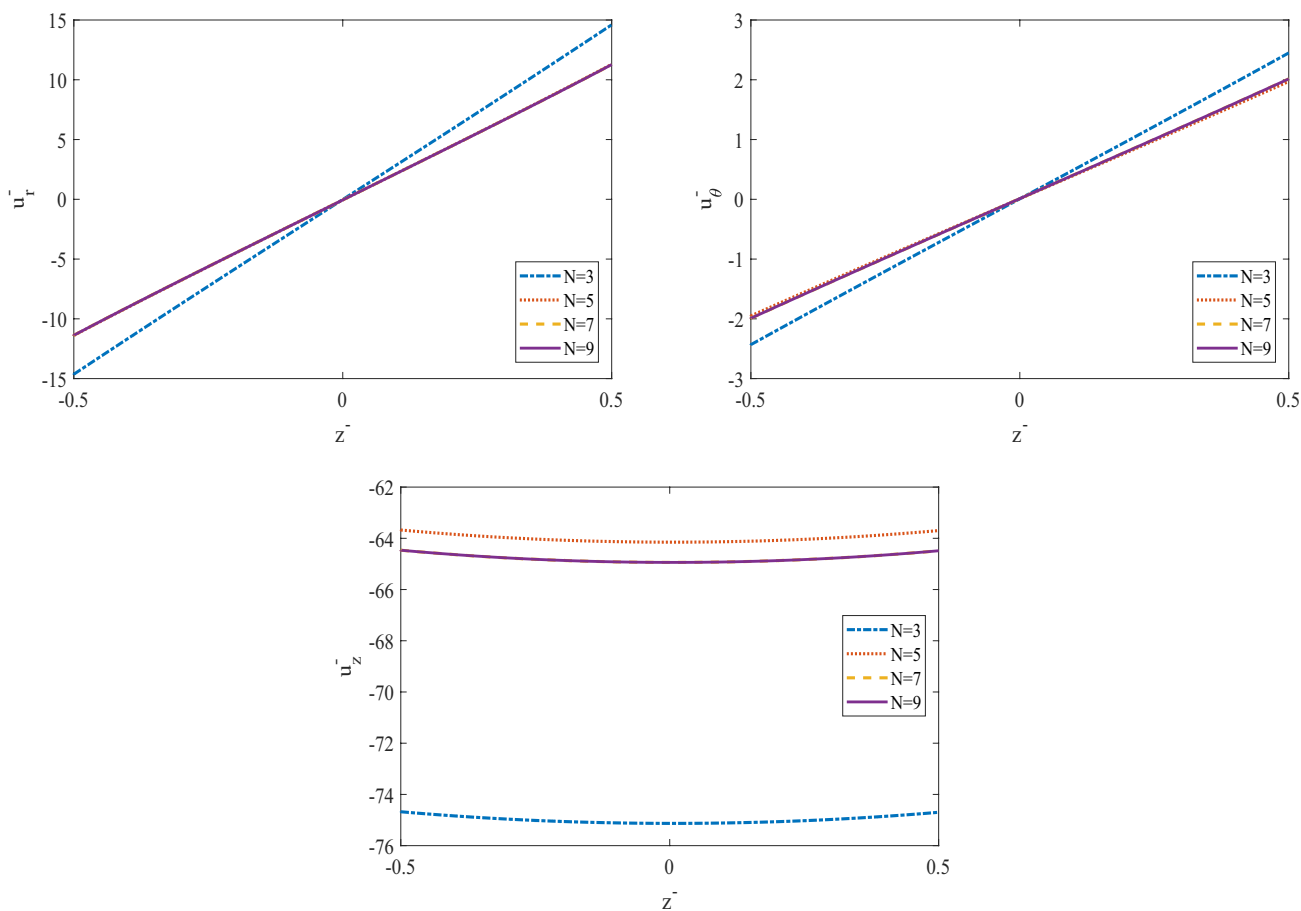


Fig. 2 (continued)

**4.1 Validation**

The properties in this validation section can be written as:

$$E(z) = E_m \left( \frac{h - 2z}{2h} \right)^n + E_c \left[ 1 - \left( \frac{h - 2z}{2h} \right)^n \right] \tag{37a}$$

$$E_r = 0.396, E_c = 125.83 \times 10^9, E_m = E_c \times E_r \tag{37b}$$

$$R_o = 1, h = 0.2 \times R_o, \nu = 0.288. \tag{37c}$$

The properties dimensionless stress and displacement in this example can be written as:

$$\bar{w}_0^F = \frac{64w_0^F D_c}{q_0 R_o^4} = \frac{D_c}{\Omega_1} \left[ 1 - \left( \frac{r}{R_o} \right)^2 \right]^2 + \frac{8}{3K_s^2 (1 - \nu_c)} \left( \frac{h}{R_o} \right)^2 \left[ 1 - \left( \frac{r}{R_o} \right)^2 \right] \left( \frac{1+n}{E_r + n} \right) \tag{37a}$$

$$\bar{u}_0^F = \frac{64u_0^F D_c}{q_0 R_o^4} = \frac{D_c}{\Omega_1} \left[ 1 - \left( \frac{r}{R_o} \right)^2 \right]^2 + \frac{8}{3K_s^2 (1 - \nu_c)} \left( \frac{h}{R_o} \right)^2 \left[ 1 - \left( \frac{r}{R_o} \right)^2 \right] \left( \frac{1+n}{E_r + n} \right) \tag{37b}$$

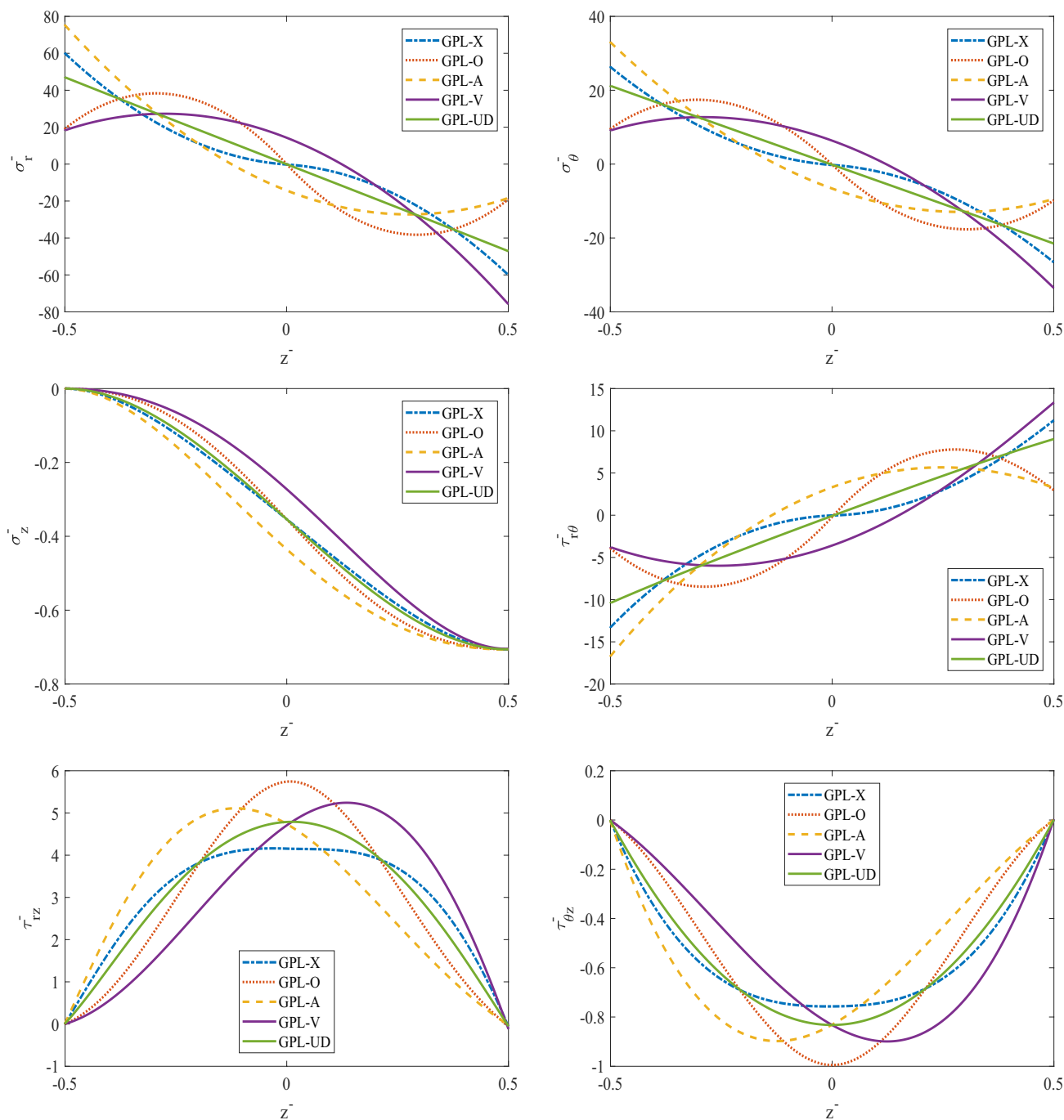


**Fig. 3** Stress and displacement fields of the FG-GPLRC annular plate for different FG patterns with  $R_o/R_i=2$ ,  $h=0.1R_i$ ,  $\Lambda_{GPL}=0.01$  wt%,  $K_{wo}=K_{po}=100$ ,  $f_1=f_2=0.1$ ,  $K_{r10}=K_{r20}=10$ ,  $\theta_0 = \pi/4$ , and Simply–Simply boundary conditions

$$\left( \bar{\sigma}_0^F, \bar{\tau}_{rz}^F \right) = \left( \frac{\sigma_0^F}{q_0}, \frac{\tau_{rz}^F}{q_0} \right). \tag{37c}$$

Table 1 presents a validation study for proving the result of the current paper. For this regard, the Non-dimensional maximum deflections in the conditions of various power

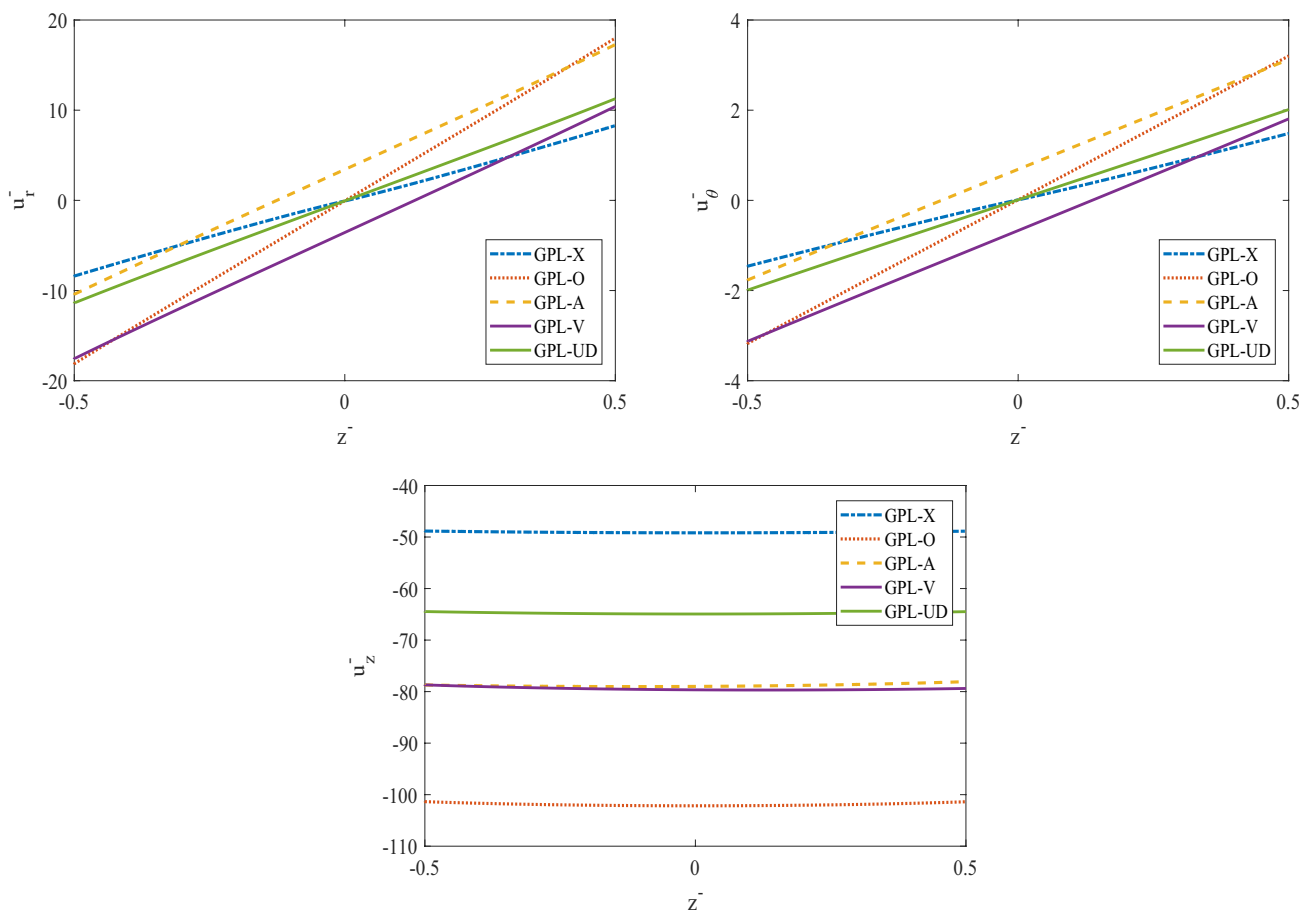


Fig. 3 (continued)

index ( $n$ ) value  $\bar{w}_0^F(0, 0)$ ,  $\bar{u}_0^F(0, -\frac{h}{2})$ ,  $\bar{\sigma}_z^F(\frac{R}{2}, 0)$  and  $\bar{\tau}_{rz}^F(R, 0)$  are compared with those outcomes in the Ref. [79]. As shown in the comparison studies, this paper’s results have a suitable agreement with the presented study in the literature. The difference between the present study and Ref. [79] using three-dimensional elasticity theory in the present study shows that this theory presents an exact method.

The impact of the  $N$  on the convergence condition is reported in Fig. 2 for investigation of bending response and stress analysis of FG-GPLRCAAP under initially stressed interacting with the gradient elastic foundations. In this regard, the static and bending behaviors of the structure are presented for four  $N$ . Based on the presented diagram in Fig. 2, we can report that when the  $N$  is more than seven, the stress and displacement fields don’t have a dependency on the number of grid points. As a conclusion from Fig. 2, the

convergence condition of the GDQ method is achieved by employing seven grid points for the semi-analytical method.

In Fig. 3 shows the influence of five kinds of GPLs patterns on the static and stress responses of the FG-GPLRC circular/annular plates under initially stressed interacting with the gradient elastic foundations. Generally, GPL-A structure has the best bending responses, but at the inner and outer layers, the structure with GPL-X and GPL-O patterns encounter us with the best static responses. In addition, the structure with the GPL-UD pattern provides the most uniform distribution of displacement and stress fields. In addition, the weakest system against bending responses is the structure with a GPL-V pattern. The normal stress in the structure with GPL-A is high, but the displacement is low. The higher shear stresses at the inner, middle, and outer layers can see in the composite disk with GPL-A, GPL-O, and GPL-V patterns.

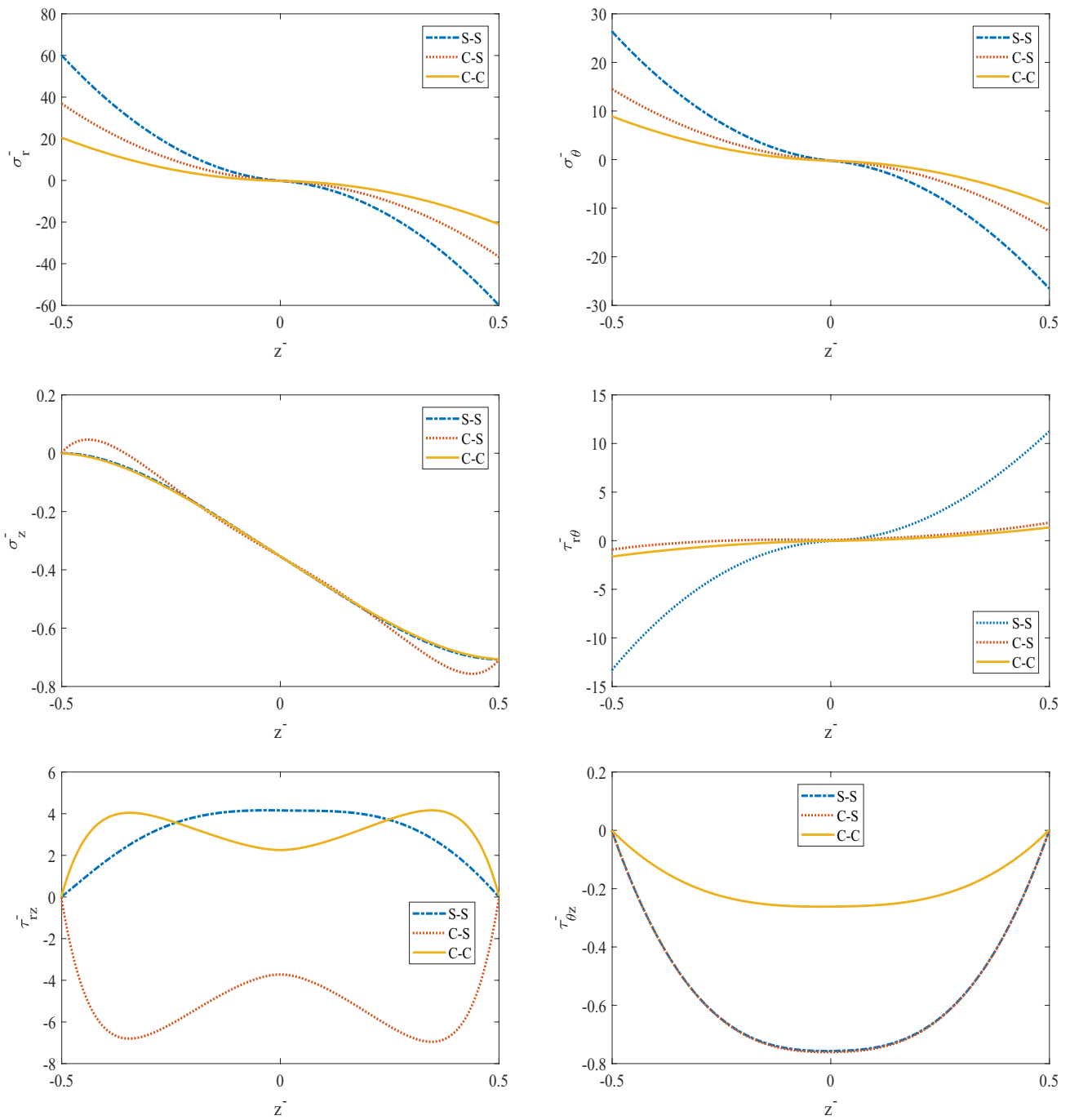


**Fig. 4** Stress and displacement fields of the structure for three kinds of boundary conditions with  $R_j/R_i=2$ ,  $h=0.1R_i$ ,  $\Lambda_{GPL}=0.01$  wt%, GPL-X,  $K_{w0}=K_{p0}=10$ ,  $f_1=f_2=0.1$ ,  $K_{r10}=K_{r20}=10$ ,  $\theta_0 = \pi/4$ , and annular plate

The static and bending behaviors of the FG-GPLRC circular/annular plates under initially stressed interacting with the gradient elastic foundations are presented in Fig. 4 by

focusing on the effect of three kinds of boundary conditions. According to Fig. 4, when the structure is encountered with the clamped edges, the better bending response

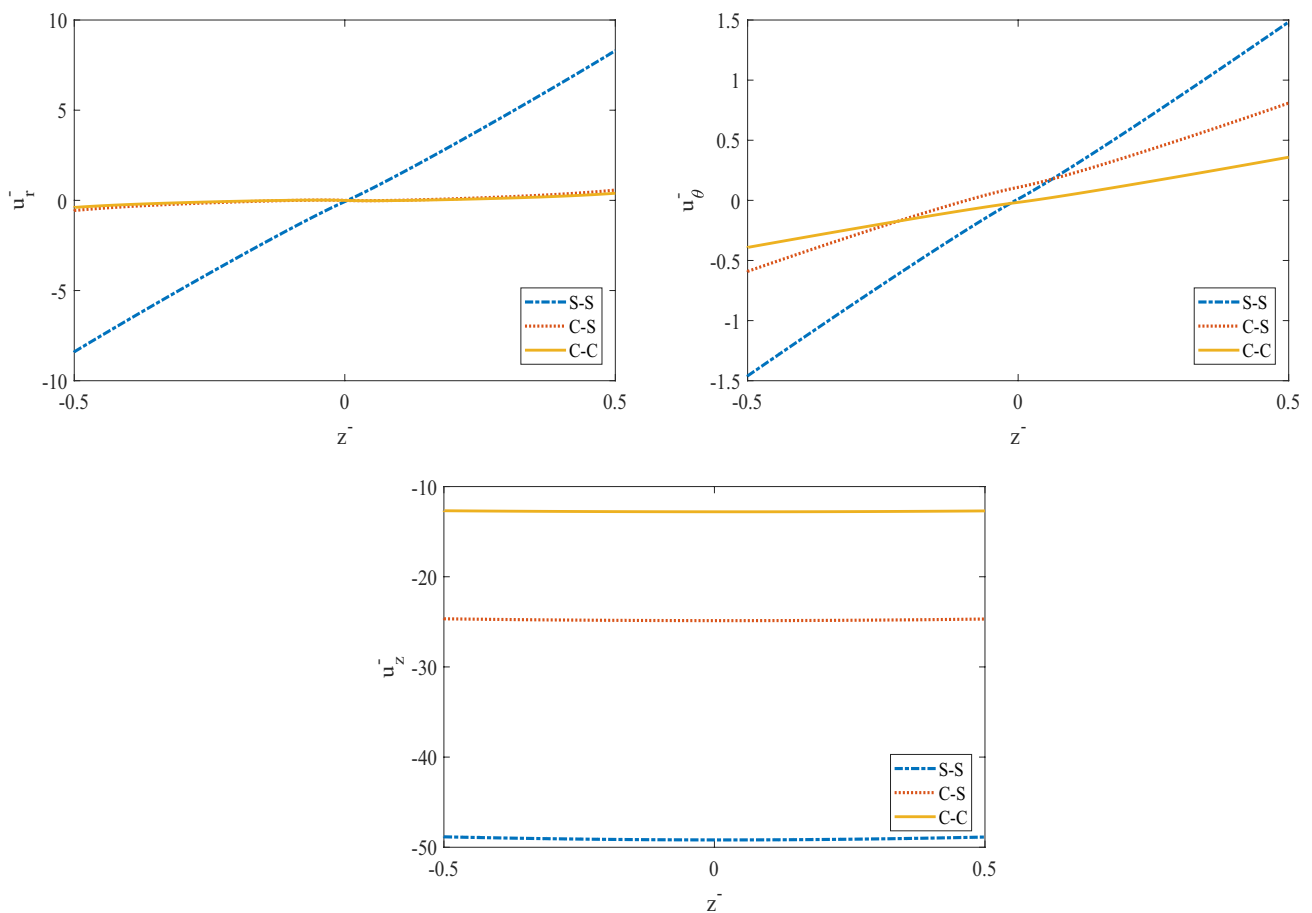
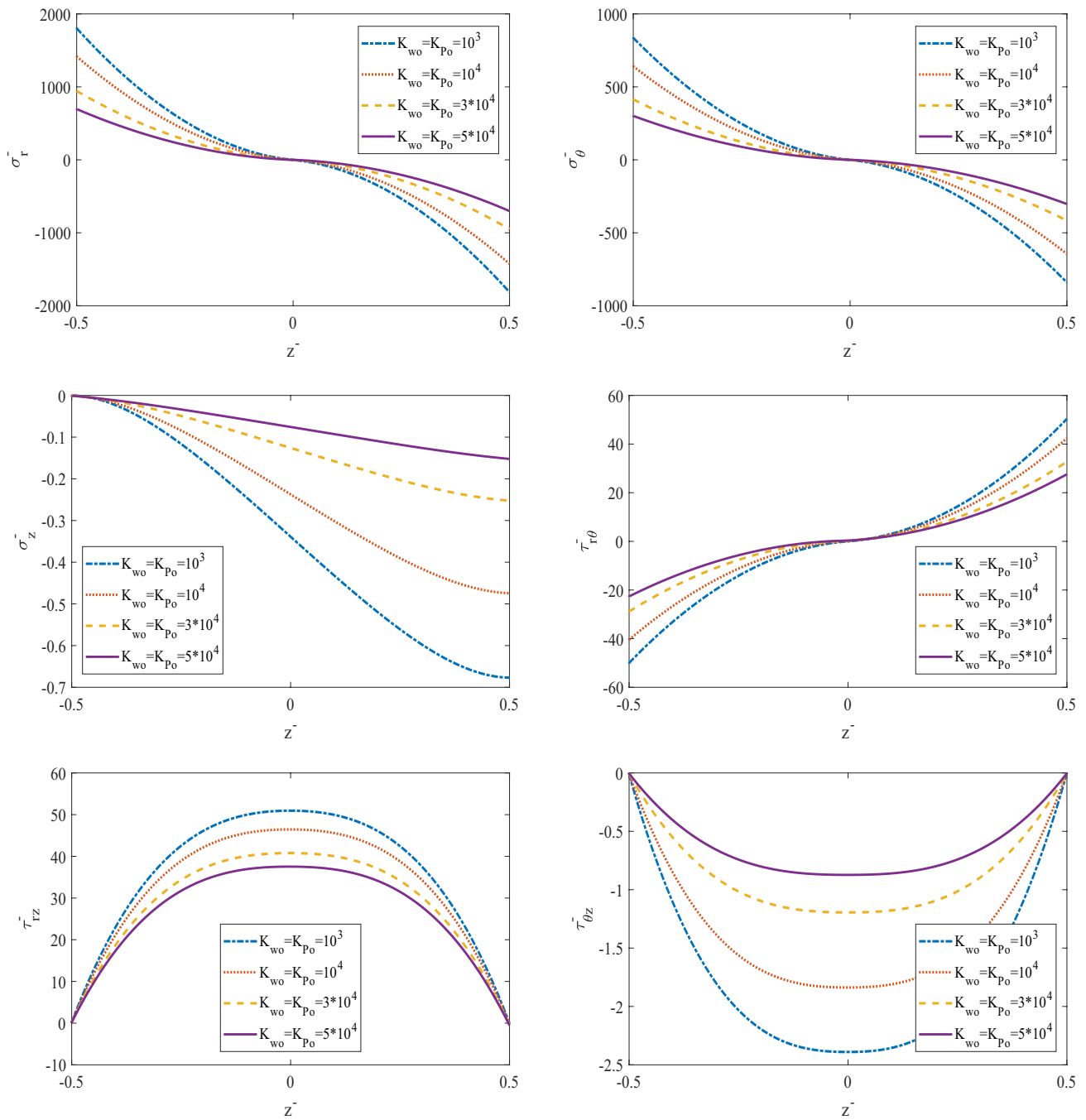


Fig. 4 (continued)

and the lowest stress are seen. In addition, in the middle layers cannot see any effect from boundary conditions on the normal axial stress, while in the inner and outer layers, when the structure is encountered with simple edges, we can see the highest axial normal stress. In addition, if the structure encounters the clamped edges (C–C and C–S boundary conditions), we cannot find a remarkable change in the radial bending response while having simply–simply edges, we can see an increase in the radial displacement field. Besides, for each boundary condition, the maximum axial shear stress is seen in the middle layers, and the structure with clamped edges has the lowest shear stress along

the thickness direction. In addition, boundary conditions on normal stress are more remarkable in the inner and outer layers. Last but not the list, bending, and static responses of the structure will improve by increasing the structure’s rigidity.

The purpose of Fig. 5 is an investigation about the effect of Winkler and Pasternak factors ( $K_{wo}$  and  $K_{po}$ ) on the stress and displacement fields of the structure. Accordingly, as the Winkler and Pasternak factors of the foundation increase, the in-plane and out plane stress decrease. Also, the impact of Winkler and Pasternak factors on the in-plane or shear stress ( $\tau_{rz}$  and  $\tau_{\theta z}$ ) is more remarkable at the middle layers. in addition, increasing the foundation



**Fig. 5** Investigation the effect of the foundation coefficients on the stress and displacement fields of the structure with  $R_o/R_i=2$ ,  $h=0.01R_i$ ,  $\Lambda_{GPL}=0.01$  wt%, GPL-X,  $f_1=f_2=0.1$ ,  $K_{r10}=K_{r20}=10$ ,  $\theta_0 = \pi/4$ , Clamped–Clamped boundary conditions, and annular plate

factors is a reason to decrease the axial stress ( $\sigma_z$ ) and this issue becomes bold by increasing  $z^-$  or at the outer layers. Furthermore, the system’s static stability and bending

behavior improve due to increasing the value of Winkler and Pasternak factors, and the stress distribution becomes more uniform.

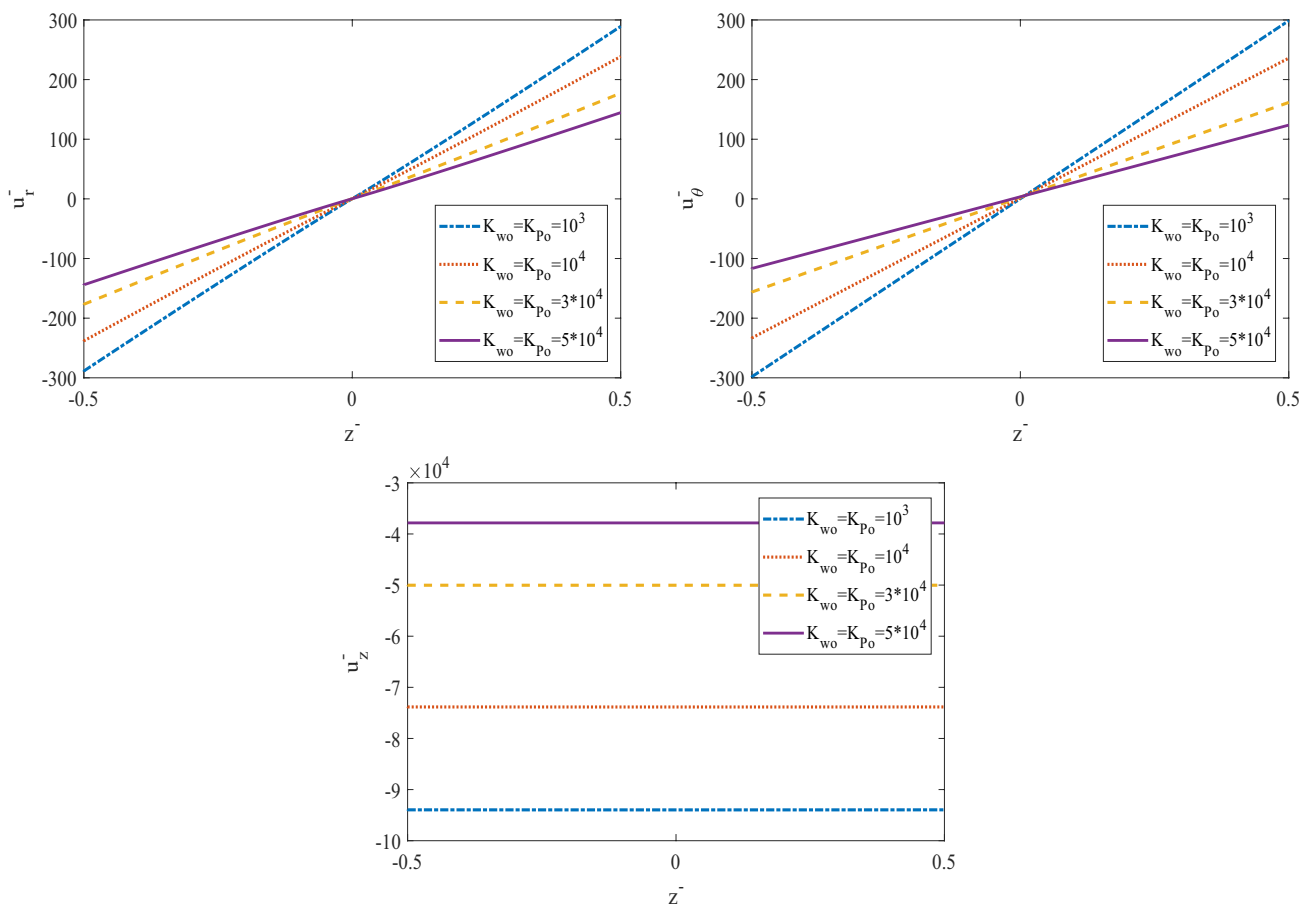
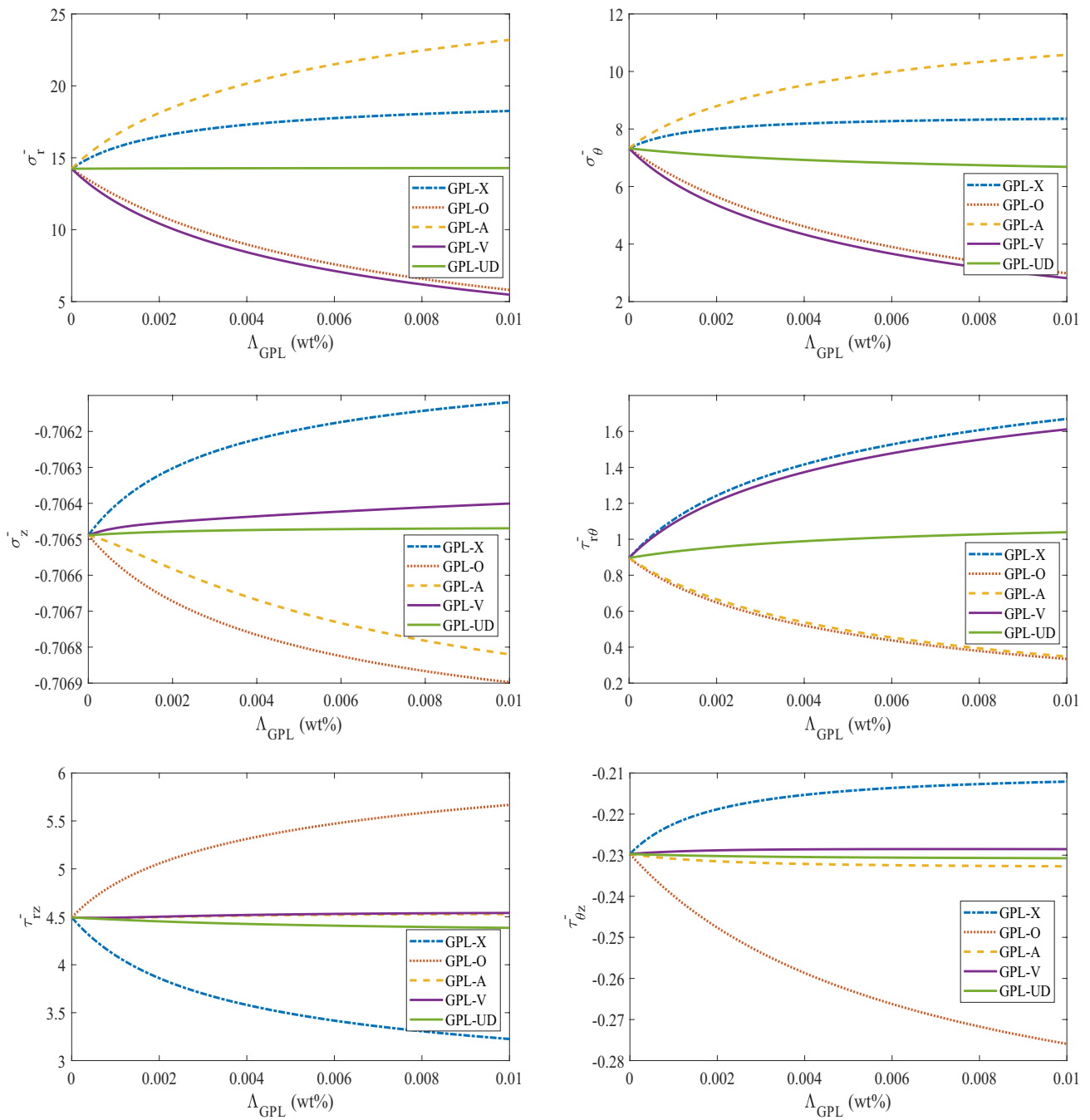


Fig. 5 (continued)

Stress and displacement fields versus to weight fraction of GPLs ( $\Lambda_{GPL}$ ) are presented in Fig. 6 for five kinds of GPLRC patterns. Generally, increasing  $\Lambda_{GPL}$  factor makes a positive impact on the structure’s static and bending behaviors, and the mentioned relation is more considerable by employing the GPL-X pattern. In addition, when the GPL-UD pattern makes the structure, the weight fraction of GPLs has the lowest positive impact on stress and displacement fields. For all patterns, as the  $\Lambda_{GPL}$  factor increases, the displacement and stress fields decrease.

The purpose of Fig. 7 is an investigation about the effect of initial or residual internal stress on the stress and displacement fields of the FG-GPLRCACP/FG-GPLRCAAP under

initially stressed interacting with the gradient elastic foundations. By having attention to Fig. 7 as the value of the initial stress increases, the system’s bending properties improve. In addition, there are no effects from internal stress on the axial stress, but other components of stress fields decrease owing to increasing the initial internal stress. In addition, the impact of residual internal stress on the hoop and axial shear stress is bold at  $-0.35 \leq z^- \leq 0.15$  and the influences of the internal stress on the displacement fields is more remarkable at the  $z^- = -0.5$  and  $0.5$ . Furthermore, the stress and displacement fields’ distribution become more uniform due to increasing the initial stress. At  $z^- = -0.5, 0$ , and  $0.5$ , we can find that initial stress doesn’t affect axial normal stress.



**Fig. 6** Maximum stress and displacement fields of the structure for the different volume fraction of GPLs with  $R_o/R_i=2$ ,  $h=0.1R_i$ ,  $K_{wo}=K_{po}=10$ ,  $f_1=f_2=0.1$ ,  $K_{r10}=K_{r20}=10$ ,  $\theta_0 = \pi/4$ ,  $\bar{\sigma}_0 = 0$ , Clamped–Clamped boundary conditions, and annular plate



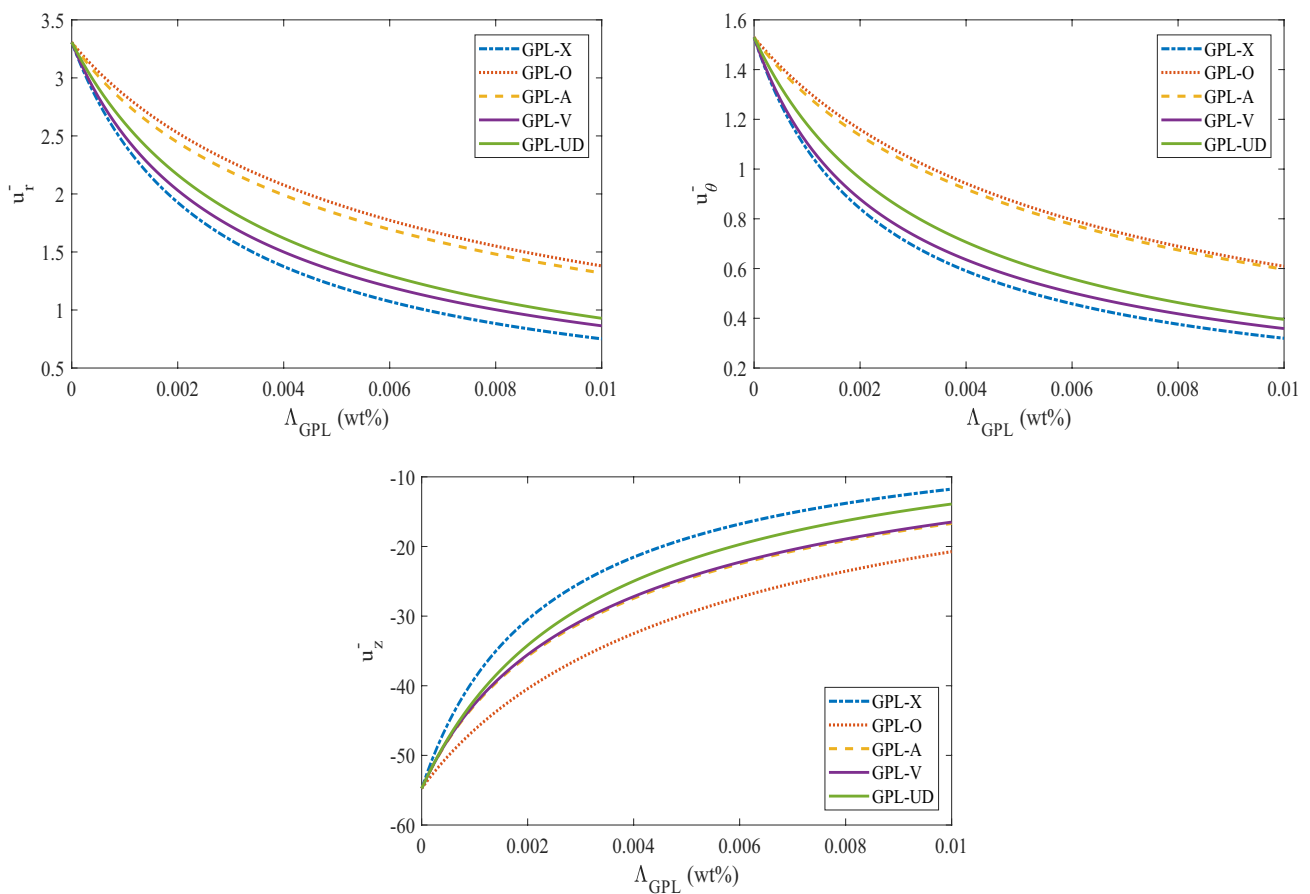
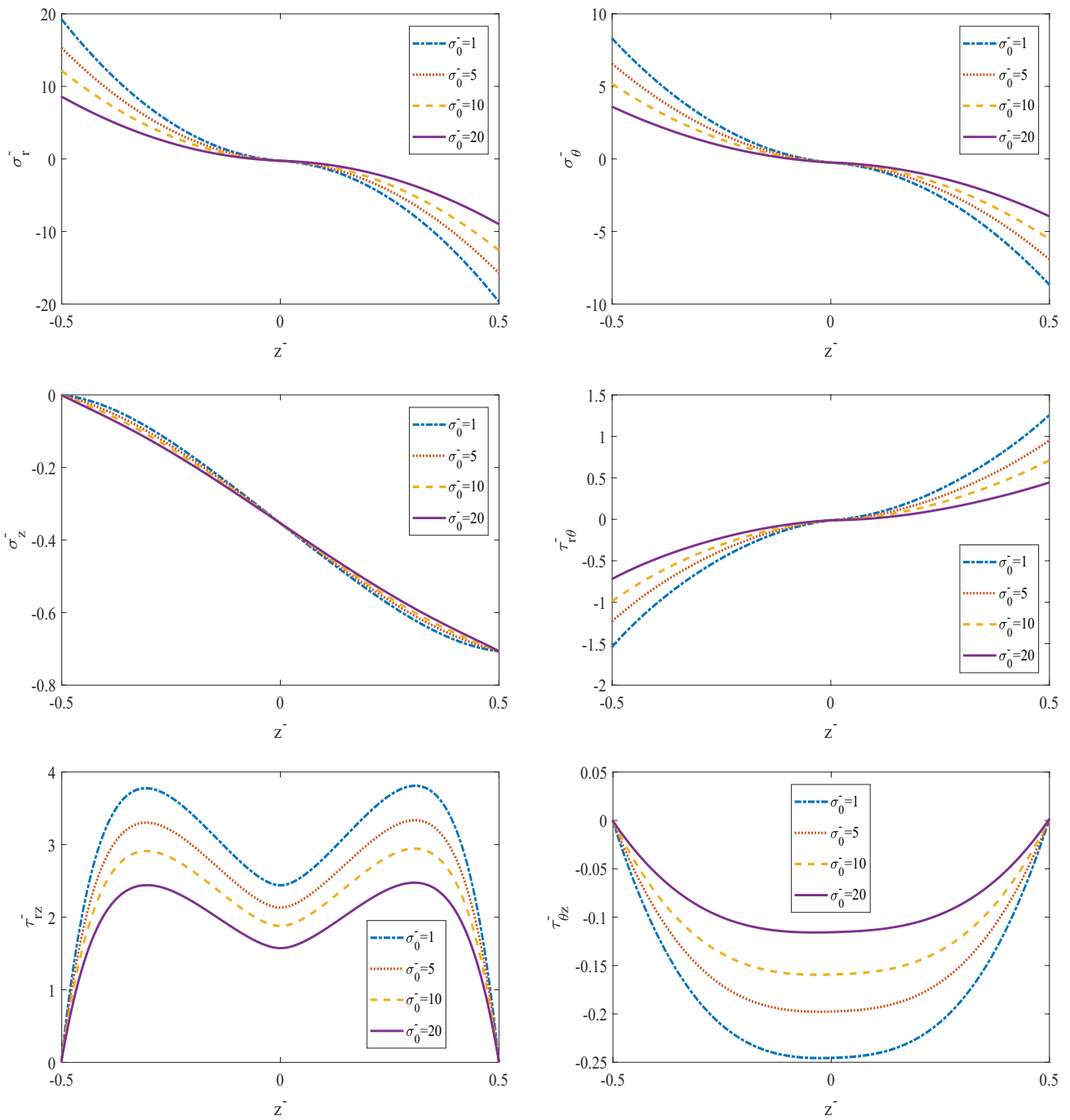


Fig. 6 (continued)

Stress and displacement fields the FG-GPLRCACP/FG-GPLRCAAP under initially stressed interacting with the gradient elastic foundations are presented in Fig. 8 by considering the effects of thickness and width of the GPLs. Generally, increasing thickness and width of the GPLs positively impact the bending behaviors of the structure. In addition, adding the length of the GPLs increases, the value of stress and displacement increases, so the system’s static stability decreases.

### 5 Conclusion

This article explored the bending response of the HLN-RACP/ HLNRAAP reinforced by GPLs resting on gradient elastic foundation within non-polynomial framework under initially stresses for different cases of boundary conditions. The main advantage is that it benefited from the exact theory (three-dimensional elasticity theory) to describe the kinematics of the structure. The numerical results were determined using the fast converging DQM. The continuity



**Fig. 7** Stress and displacement fields of the structure for Effect of initially stressed with  $R_o/R_i=2$ ,  $h=0.1R_i$ ,  $\Lambda_{GPL}=0.01$  wt%, GPL-X,  $K_{wo}=K_{po}=10$ ,  $f_1=f_2=0.1$ ,  $K_{r10}=K_{r20}=10$ ,  $\theta_0 = \pi/4$ , and clamped–clamped annular plate

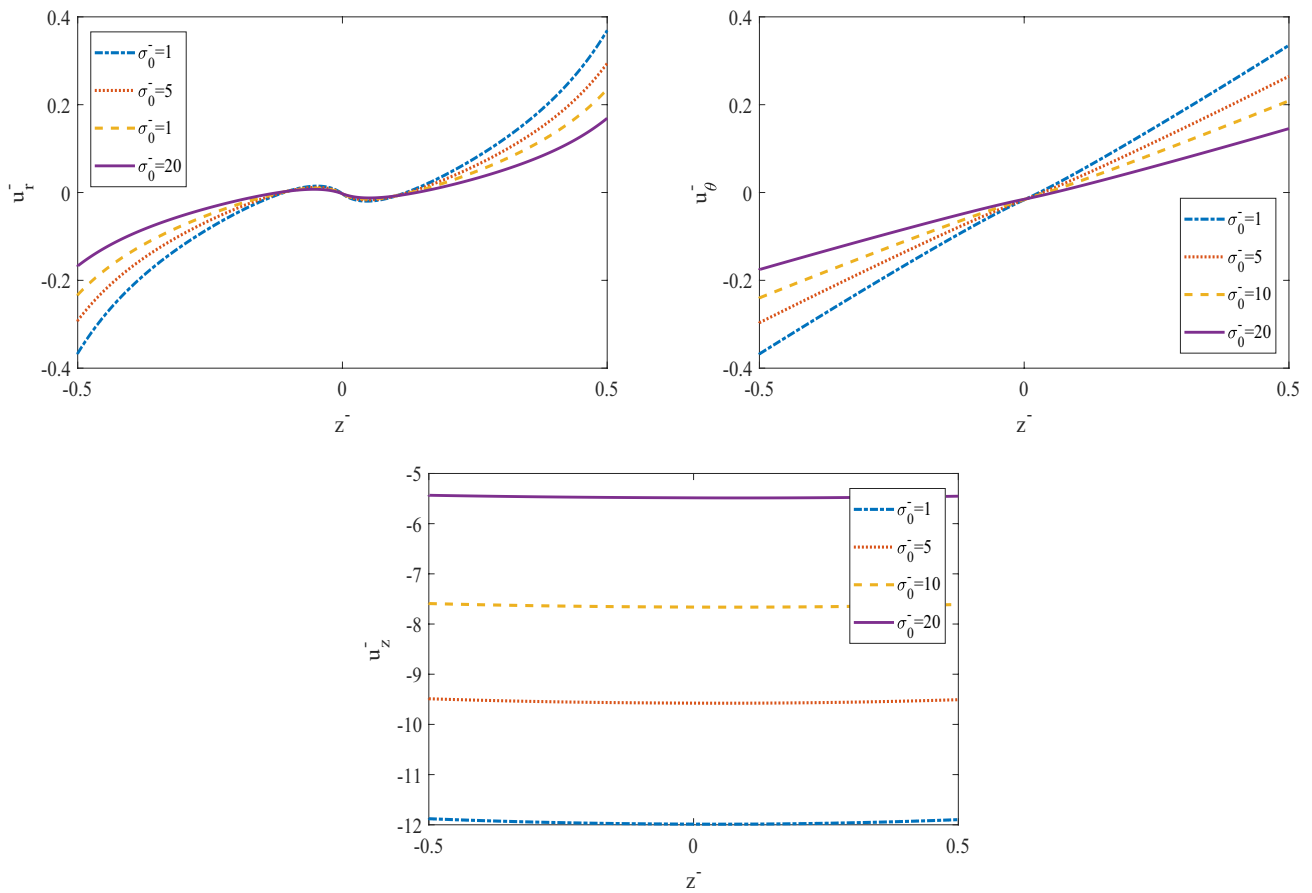
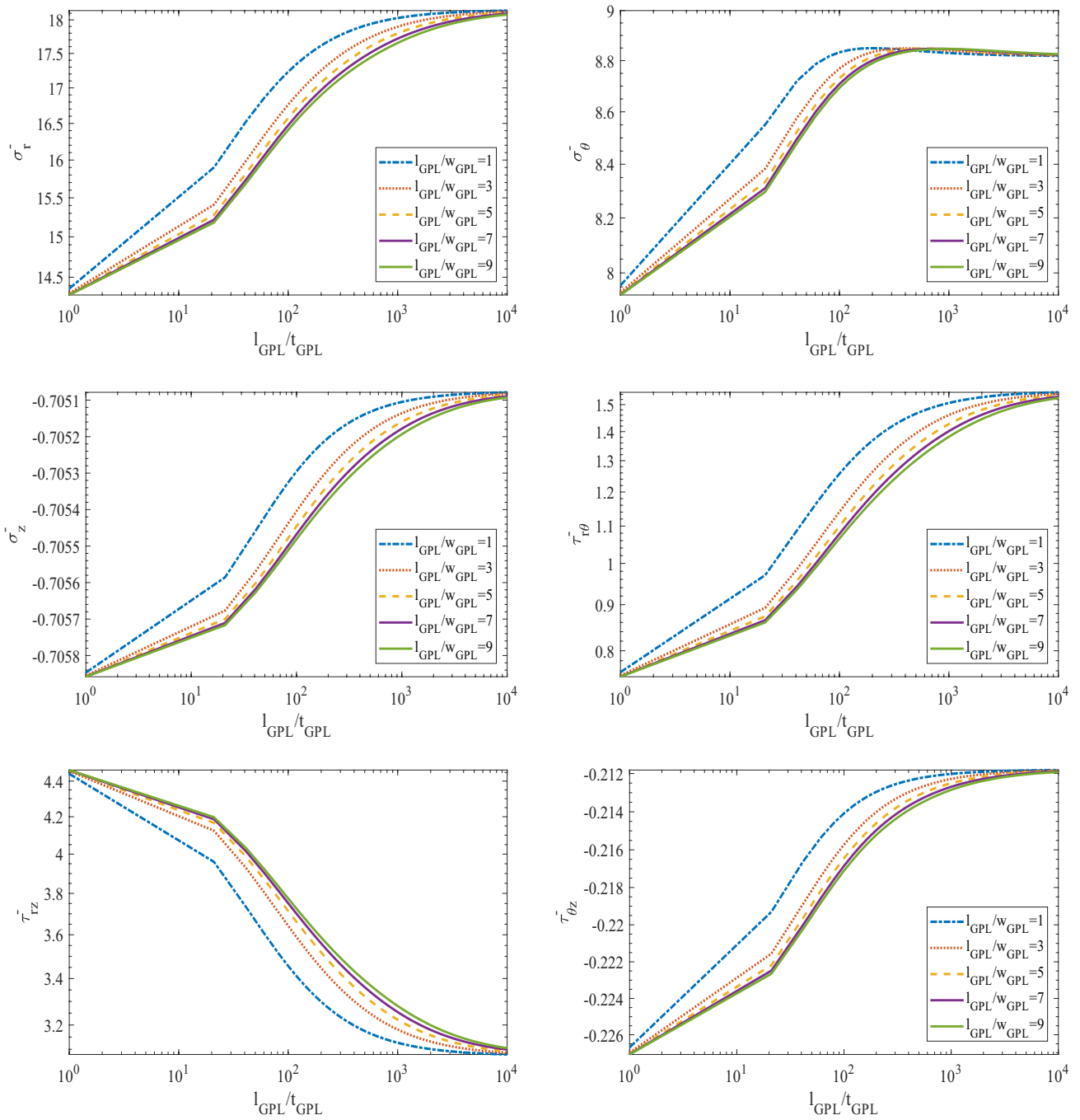


Fig. 7 (continued)

condition was considered between each of the heterogeneous sections to satisfy the equality of displacement terms at the contact surfaces. Finally, the most bolded results of this paper were as follows:

- Among the five GPL distribution patterns considered in the present study, GPL-X works more effectively and results in the smallest displacement and stress, also GPL-O has the highest displacement and stress.
- As the  $\Lambda_{GPL}$  parameter increases the bending response in the structure improves.
- When the structure is encountered with the clamped edges, the better bending response and the lowest stress happens in the sandwich disk.
- The system’s static stability and bending behavior improve due to increasing the value of Winkler and Pasternak factors, and the stress distribution becomes more uniform.
- Increasing the thickness and width of the GPLs positively impacts the bending behaviors of the structure. In addition, adding the length of the GPLs increases, the value of stress and displacement increases, so the system’s static stability decreases.



**Fig. 8** Stress and displacement fields of the structure for size effect of graphene with  $R_o/R_i=2$ ,  $h=0.1R_i$ ,  $\Lambda_{GPL}=0.01$  wt%, GPL-X,  $K_{wo}=K_{po}=10$ ,  $f_1=f_2=0.1$ ,  $K_{r10}=K_{r20}=10$ ,  $\theta_0 = \pi/4$ , clamped-clamped boundary conditions, and annular plate

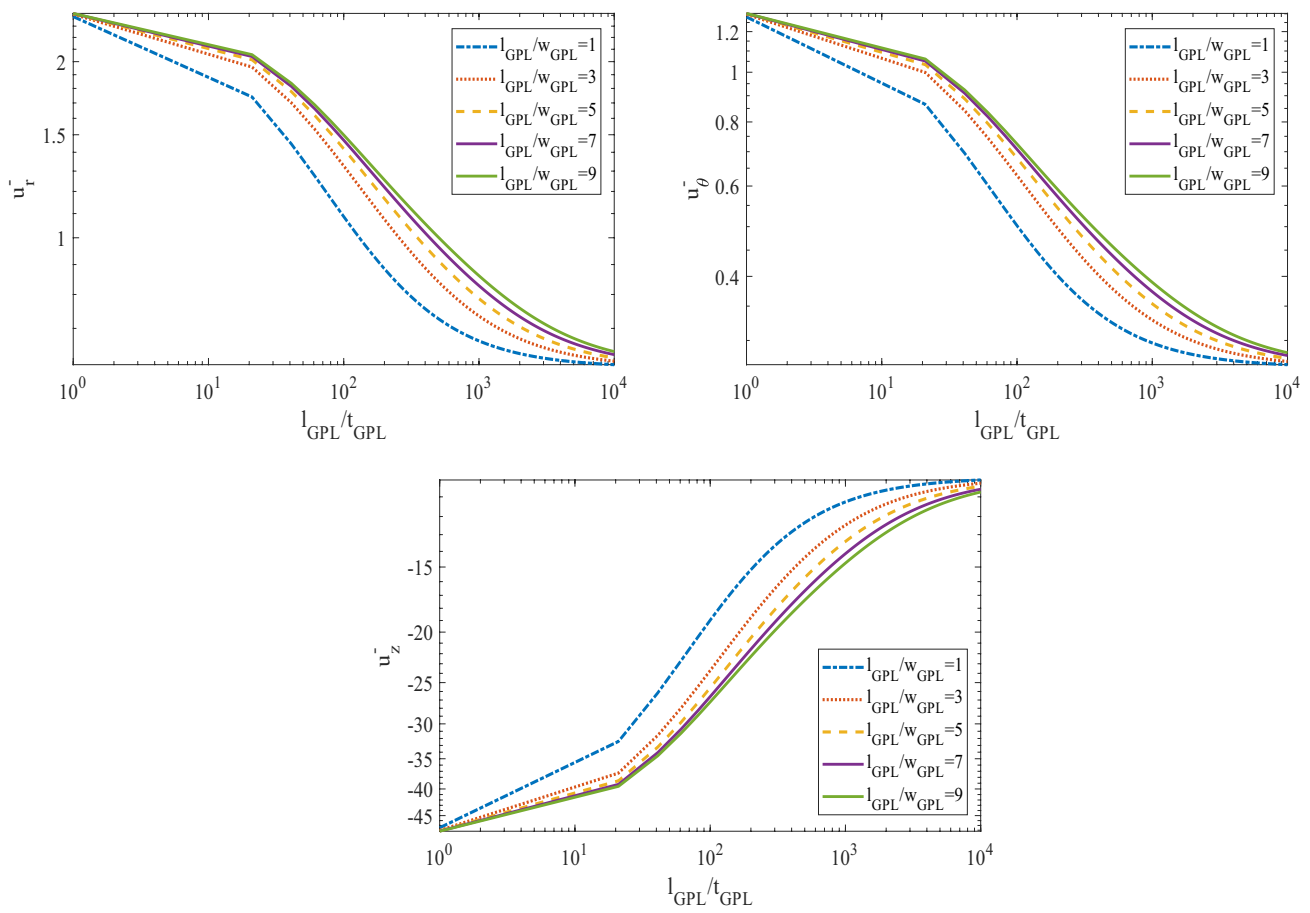


Fig. 8 (continued)

## References

- Chen S, Hassanzadeh-Aghdam M, Ansari R (2018) An analytical model for elastic modulus calculation of SiC whisker-reinforced hybrid metal matrix nanocomposite containing SiC nanoparticles. *J Alloy Compd* 767:632–641
- Abedini M, Zhang C (2020) Performance assessment of concrete and steel material models in LS-DYNA for enhanced numerical simulation, a state of the art review. *Arch Comput Methods Eng*. <https://doi.org/10.1007/s11831-020-09483-5>
- Zhang C, Mousavi AA (2020) Blast loads induced responses of RC structural members: state-of-the-art review. *Compos Part B Eng*. <https://doi.org/10.1016/j.compositesb.2020.108066>
- Li C, Sun L, Xu Z, Wu X, Liang T, Shi W (2020) Experimental investigation and error analysis of high precision fbg displacement sensor for structural health monitoring. *Int J Struct Stab Dyn*. <https://doi.org/10.1142/S0219455420400118>
- Zhang C, Alam Z, Sun L, Su Z, Samali B (2019) Fibre Bragg grating sensor-based damage response monitoring of an asymmetric reinforced concrete shear wall structure subjected to progressive seismic loads. *Struct Control Health Monit* 26(3):e2307
- Zhang C, Ou J (2015) Modeling and dynamical performance of the electromagnetic mass driver system for structural vibration control. *Eng Struct* 82:93–103
- Zheng J, Zhang C, Li A (2020) Experimental investigation on the mechanical properties of curved metallic plate dampers. *Appl Sci* 10(1):269
- Abedini M, Mutalib AA, Zhang C, Mehrmashhadi J, Raman SN, Alipour R, Momeni T, Mussa MH (2020) Large deflection behavior effect in reinforced concrete columns exposed to extreme dynamic loads. *Front Struct Civ En* 14(2):532–553
- Zhang Y, Zhang X, Li M, Liu Z (2019) Research on heat transfer enhancement and flow characteristic of heat exchange surface in cosine style runner. *Heat Mass Transf* 55(11):3117–3131
- Khosravi R, Teymourtash A, Fard MP, Rabiei S, Bahiraei M (2020) Numerical study and optimization of thermohydraulic characteristics of a graphene–platinum nanofluid in finned annulus using genetic algorithm combined with decision-making technique. *Eng Comput*. <https://doi.org/10.1007/s00366-020-01178-6>
- Rafiee MA, Rafiee J, Wang Z, Song H, Yu Z-Z, Koratkar N (2009) Enhanced mechanical properties of nanocomposites at low graphene content. *ACS Nano* 3(12):3884–3890
- Esmailpoor Hajilak Z, Pourghader J, Hashemabadi D, Sharifi Bagh F, Habibi M, Safarpour H (2019) Multilayer GPLRC composite cylindrical nanoshell using modified strain gradient theory. *Mech Based Des Struct Mach* 47(5):521–545
- Al-Furjan MSH, Moghadam SA, Dehini R, Shan L, Habibi M, Safarpour H (2020) Vibration control of a smart shell reinforced by graphene nanoplatelets under external load: Semi-numerical and finite element modeling. *Thin-Walled Struct* 107:242. <https://doi.org/10.1016/j.tws.2020.107242>

14. Ebrahimi F, Habibi M, Safarpour H (2019) On modeling of wave propagation in a thermally affected GNP-reinforced imperfect nanocomposite shell. *Eng Comput* 35(4):1375–1389
15. Habibi M, Taghdir A, Safarpour H (2019) Stability analysis of an electrically cylindrical nanoshell reinforced with graphene nanoplatelets. *Compos B Eng* 175:107125
16. Safarpour H, Hajilak ZE, Habibi M (2019) A size-dependent exact theory for thermal buckling, free and forced vibration analysis of temperature dependent FG multilayer GPLRC composite nanostructures resting on elastic foundation. *Int J Mech Mater Des* 15(3):569–583
17. Al-Furjan M, Habibi M, Ghabussi A, Safarpour H, Safarpour M, Tounsi A (2020) Non-polynomial framework for stress and strain response of the FG-GPLRC disk using three-dimensional refined higher-order theory. *Eng Struct*, p 111496
18. Pourjabari A, Hajilak ZE, Mohammadi A, Habibi M, Safarpour H (2019) Effect of porosity on free and forced vibration characteristics of the GPL reinforcement composite nanostructures. *Comput Math Appl* 77(10):2608–2626
19. Safarpour M, Ghabussi A, Ebrahimi F, Habibi M, Safarpour H (2020) Frequency characteristics of FG-GPLRC viscoelastic thick annular plate with the aid of GDQM. *Thin-Walled Struct* 150:106683. <https://doi.org/10.1016/j.tws.2020.106683>
20. Ebrahimi F, Hashemabadi D, Habibi M, Safarpour H (2020) Thermal buckling and forced vibration characteristics of a porous GNP reinforced nanocomposite cylindrical shell. *Microsyst Technol* 26(2):461–473
21. Habibi M, Hashemabadi D, Safarpour H (2019) Vibration analysis of a high-speed rotating GPLRC nanostructure coupled with a piezoelectric actuator. *Eur Phys JPlus* 134(6):307
22. Tam M, Yang Z, Zhao S, Zhang H, Zhang Y, Yang J (2020) Non-linear bending of elastically restrained functionally graded graphene nanoplatelet reinforced beams with an open edge crack. *Thin-Walled Struct* 156:106972
23. Li Y, Li S, Guo K, Fang X, Habibi M (2020) On the modeling of bending responses of graphene-reinforced higher order annular plate via two-dimensional continuum mechanics approach. *Eng Comput*. <https://doi.org/10.1007/s00366-020-01166-w>
24. Liu D, Zhou Y, Zhu J (2021) On the free vibration and bending analysis of functionally graded nanocomposite spherical shells reinforced with graphene nanoplatelets: three-dimensional elasticity solutions. *Eng Struct* 226:111376. <https://doi.org/10.1016/j.engstruct.2020.111376>
25. Ghabussi A, Marnani JA, Rohanimanesh MS Improving seismic performance of portal frame structures with steel curved dampers. In: *Structures*, 2020. Elsevier, pp 27–40. <https://doi.org/10.1016/j.istruc.2019.12.025>
26. Ma X, Foong LK, Morasaei A, Ghabussi A, Lyu Z (2020) Swarm-based hybridizations of neural network for predicting the concrete strength. *Smart Struct Syst* 26(2):241–251
27. Onsorynezhad S, Abedini A, Wang F (2018) Analytical study of a piezoelectric frequency up-conversion harvester under sawtooth wave excitation. In: *Dynamic Systems and Control Conference*, 2018. American Society of Mechanical Eng, p V002T018A004
28. Chen H, Zhang G, Fan D, Fang L, Huang L (2020) Nonlinear lamb wave analysis for microdefect identification in mechanical structural health assessment. *Measurement*, pp 108026
29. Zhang W (2020) Parameter adjustment strategy and experimental development of hydraulic system for wave energy power generation. *Symmetry* 12(5):711
30. Mou B, Zhao F, Qiao Q, Wang L, Li H, He B, Hao Z (2019) Flexural behavior of beam to column joints with or without an overlying concrete slab. *Eng Struct* 199:109616
31. Mou B, Li X, Bai Y, Wang L (2019) Shear behavior of panel zones in steel beam-to-column connections with unequal depth of outer annular stiffener. *J Struct Eng* 145(2):04018247
32. Mou B, Bai Y (2018) Experimental investigation on shear behavior of steel beam-to-CFST column connections with irregular panel zone. *Eng Struct* 168:487–504
33. Liu J, Yi Y, Wang X (2020) Exploring factors influencing construction waste reduction: a structural equation modeling approach. *J Clean Prod* 276:123185
34. Lv Z, Qiao L (2020) Deep belief network and linear perceptron based cognitive computing for collaborative robots. *Appl Soft Comput*. <https://doi.org/10.1016/j.asoc.2020.106300>
35. Li Z, Liu H, Dun Z, Ren L, Fang J (2020) Grouting effect on rock fracture using shear and seepage assessment. *Constr Build Mater* 242:118131
36. Alam Z, Zhang C, Samali B (2020) Influence of seismic incident angle on response uncertainty and structural performance of tall asymmetric structure. *Struct Des Tall Sp Build*. <https://doi.org/10.1002/tal.1750>
37. Alam Z, Zhang C, Samali B (2020) The role of viscoelastic damping on retrofitting seismic performance of asymmetric reinforced concrete structures. *Earthq Eng Vib* 19(1):223–237
38. Zhang C, Wang H (2020) Swing vibration control of suspended structures using the Active Rotary Inertia Driver system: theoretical modeling and experimental verification. *StructControl Health Monit* 27(6):e2543
39. Zhang C, Wang H (2019) Robustness of the active rotary inertia driver system for structural swing vibration control subjected to multi-type hazard excitations. *Appl Sci* 9(20):4391
40. Kordestani H, Zhang C, Shadabfar M (2020) Beam damage detection under a moving load using random decrement technique and Savitzky-Golay Filter. *Sensors* 20(1):243
41. Yang J, Chen D, Kitipornchai S (2018) Buckling and free vibration analyses of functionally graded graphene reinforced porous nanocomposite plates based on Chebyshev-Ritz method. *Compos Struct* 193:281–294. <https://doi.org/10.1016/j.compstruct.2018.03.090>
42. Gibson I, Ashby MF (1982) The mechanics of three-dimensional cellular materials. *Proc R Soc Lond A Math Phys Sci* 382(1782):43–59. <https://doi.org/10.1098/rspa.1982.0088>
43. Sadd MH (2009) *Elasticity: theory, applications, and numerics*. Academic Press, London
44. Zhang C, Abedini M, Mehrmashhadi J (2020) Development of pressure-impulse models and residual capacity assessment of RC columns using high fidelity Arbitrary Lagrangian-Eulerian simulation. *Eng Struct* 224:111219
45. Sun L, Li C, Zhang C, Liang T, Zhao Z (2019) The strain transfer mechanism of fiber bragg grating sensor for extra large strain monitoring. *Sensors* 19(8):1851
46. Zhang C, Gholipour G, Mousavi AA (2019) Nonlinear dynamic behavior of simply-supported RC beams subjected to combined impact-blast loading. *Eng Struct* 181:124–142
47. Gholipour G, Zhang C, Mousavi AA (2020) Numerical analysis of axially loaded RC columns subjected to the combination of impact and blast loads. *Eng Struct* 219:110924
48. Mousavi AA, Zhang C, Masri SF, Gholipour G (2020) Structural damage localization and quantification based on a CEEMDAN Hilbert transform neural network approach: a model steel truss bridge case study. *Sensors* 20(5):1271
49. Li Z, Zhou H, Hu D, Zhang C (2020) Yield criterion for rock-like geomaterials based on strain energy and CMP model. *Int J Geomech* 20(3):04020013
50. Huang Z, Zheng H, Guo L, Mo D (2020) Influence of the position of artificial boundary on computation accuracy of conjugated infinite element for a finite length cylindrical shell. *Acoust Austral* 48(2):287–294
51. Zhang C, Gholipour G, Mousavi AA (2020) State-of-the-art review on responses of RC structures subjected to lateral impact loads. *Arch Comput Methods Eng*, pp 1–31

52. Reddy JN (2003) Mechanics of laminated composite plates and shells: theory and analysis. CRC Press, Boca Roton
53. Ghayesh MH (2019) Asymmetric viscoelastic nonlinear vibrations of imperfect AFG beams. *Appl Acoust* 154:121–128
54. Gholipour A, Ghayesh MH, Zhang Y (2020) A comparison between elastic and viscoelastic asymmetric dynamics of elastically supported AFG beams. *Vibration* 3(1):3–17
55. Gholipour A, Ghayesh MH, Hussain S (2020) A continuum viscoelastic model of Timoshenko NSGT nanobeams. *Eng Comput*. <https://doi.org/10.1007/s00366-020-01017-8>
56. Ghayesh MH (2019) Dynamical analysis of multilayered cantilevers. *Commun Nonlinear Sci Numer Simul* 71:244–253
57. Farokhi H, Ghayesh MH, Gholipour A (2017) Dynamics of functionally graded micro-cantilevers. *Int J Eng Sci* 115:117–130
58. Ghayesh MH (2018) Dynamics of functionally graded viscoelastic microbeams. *Int J Eng Sci* 124:115–131. <https://doi.org/10.1016/j.ijengsci.2017.11.004>
59. Ghayesh MH, Farokhi H (2020) Extremely large dynamics of axially excited cantilevers. *Thin-Walled Struct*. <https://doi.org/10.1016/j.tws.2019.106275>
60. Farokhi H, Ghayesh MH (2020) Extremely large-amplitude dynamics of cantilevers under coupled base excitation. *Eur J Mech A/Solids* 81:103953
61. Ghayesh MH (2018) Functionally graded microbeams: simultaneous presence of imperfection and viscoelasticity. *Int J Mech Sci* 140:339–350. <https://doi.org/10.1016/j.ijmecsci.2018.02.037>
62. Safarpour M, Rahimi A, Alibeigloo A, Bisheh H, Forooghi A (2019) Parametric study of three-dimensional bending and frequency of FG-GPLRC porous circular and annular plates on different boundary conditions. *Mech Based Des Struct Mach*. <https://doi.org/10.1080/15397734.2019.1701491>
63. Zhu Q (2019) Research on road traffic situation awareness system based on image big data. *IEEE Intell Syst* 35(1):18–26
64. Zuo C, Sun J, Li J, Asundi A, Chen Q (2020) Wide-field high-resolution 3d microscopy with fourier ptychographic diffraction tomography. *Opt Lasers Eng* 128:106003
65. Long Q, Wu C, Wang X (2015) A system of nonsmooth equations solver based upon subgradient method. *Appl Math Comput* 251:284–299
66. Zhu J, Shi Q, Wu P, Sheng Z, Wang X (2018) Complexity analysis of prefabrication contractors' dynamic price competition in mega projects with different competition strategies. *Complexity*. <https://doi.org/10.1155/2018/5928235>
67. Wu T, Xiong L, Cheng J, Xie X (2020) New results on stabilization analysis for fuzzy semi-Markov jump chaotic systems with state quantized sampled-data controller. *Inf Sci* 521:231–250
68. Liu J, Wu C, Wu G, Wang X (2015) A novel differential search algorithm and applications for structure design. *Appl Math Comput* 268:246–269
69. Lv Z, Xiu W (2019) Interaction of edge-cloud computing based on SDN and NFV for next generation IoT. *IEEE Internet Things J*. <https://doi.org/10.1109/JIOT.2019.2942719>
70. Li T, Xu M, Zhu C, Yang R, Wang Z, Guan Z (2019) A deep learning approach for multi-frame in-loop filter of HEVC. *IEEE Trans Image Process* 28(11):5663–5678
71. Cao B, Zhao J, Gu Y, Fan S, Yang P (2019) Security-aware industrial wireless sensor network deployment optimization. *IEEE Trans Ind Inf* 16(8):5309–5316
72. Gholipour G, Zhang C, Mousavi AA (2020) Nonlinear numerical analysis and progressive damage assessment of a cable-stayed bridge pier subjected to ship collision. *Mar Struct* 69:102662. <https://doi.org/10.1016/j.marstruc.2019.102662>
73. Shu C (2012) Differential quadrature and its application in engineering. Springer Science & Business Media, Berlin
74. Ghabussi A, Habibi M, Noormohammadi Arani O, Shavalipour A, Moayedi H, Safarpour H (2020) Frequency characteristics of a viscoelastic graphene nanoplatelet-reinforced composite circular microplate. *J Vib Control*. <https://doi.org/10.1177/1077546320923930>
75. Alam Z, Sun L, Zhang C, Su Z, Samali B (2020) Experimental and numerical investigation on the complex behaviour of the localised seismic response in a multi-storey plan-asymmetric structure. *Struct Infrastruct Eng*. <https://doi.org/10.1080/15732479.2020.1730914>
76. Zhu L, Kong L, Zhang C (2020) Numerical study on hysteretic behaviour of horizontal-connection and energy-dissipation structures developed for prefabricated shear walls. *Appl Sci* 10(4):1240
77. Wu H, Kitipornchai S, Yang J (2017) Thermal buckling and postbuckling of functionally graded graphene nanocomposite plates. *Mater Des* 132:430–441. <https://doi.org/10.1016/j.matdes.2017.07.025>
78. Jabbari M, Karampour S, Eslami M (2013) Steady state thermal and mechanical stresses of a poro-piezo-FGM hollow sphere. *Meccanica* 48(3):699–719
79. Reddy J, Wang C, Kitipornchai S (1999) Axisymmetric bending of functionally graded circular and annular plates. *Eur J Mech-A/Solids* 18(2):185–199. [https://doi.org/10.1016/S0997-7538\(99\)80011-4](https://doi.org/10.1016/S0997-7538(99)80011-4)

**Publisher's note** Springer Nature remains neutral with regard to jurisdictional claims in published maps and institutional affiliations.